ORIGINAL ARTICLE

Semi-confined blast loading: experiments and simulations of internal detonations

M. Kristoffersen[1] · F. Casadei[2] · G. Valsamos[2] · M. Larcher[2] · K. O. Hauge[3] · A. Minoretti[4] · T. Børvik[1,3]

Abstract

Far-field blast loading has been studied extensively for decades. Close-in, confined, and semi-confined detonations less so, partly because it is difficult to obtain good experimental data. The increase in computational power in recent years has made it possible to conduct studies of this kind numerically, but the results of such simulations ultimately depend on experimental validation and verification. This work thus aims at using reliable experiments to validate and verify numerical models developed to represent blast loading in general. Test rigs consisting of massive steel cylinders with pressure sensors were used to measure the pressure profiles of semi-confined detonations with different charge sizes. The experimental data set was then used to assess numerical models appropriate for simulating blast loading. In general, the numerical results were in excellent agreement with the experimental data, in both qualitative and quantitative terms. These results may in turn be used to analyse structures exposed to internal blast loads, which constitutes the next phase of this research project.

1 Introduction

Explosions, whether accidental or intended, pose a serious threat to structures. Damage to critical infrastructures, such as in the energy and transport sectors, like power plants, bridges or tunnels, may be particularly harmful and crippling to society. Reducing vulnerabilities and strengthening the resilience of critical infrastructures are both essential for vital societal

✉ M. Kristoffersen
martin.kristoffersen@ntnu.no

1 Structural Impact Laboratory (SIMLab), Department of Structural Engineering, NTNU, Trondheim, Norway

2 Directorate for Space, Security and Migration, Joint Research Centre (JRC), European Commission (EC), Ispra, Italy

3 Norwegian Defence Estates Agency, Oslo, Norway

4 Norwegian Public Roads Administration, Trondheim, Norway

functions and the economic activities in the internal market, forcing the policy makers to take actions in that direction, as for example through the CER directive [1] at the EU level. In cases where the detonation occurs internally to a structure, i.e., a blast completely or partially confined by the structure, the result may be catastrophic collapse of the structure [2]. Thus, being able to accurately represent the shock load arising from an internal detonation is vital to engineers designing structures prone to such extreme load scenarios.

A typical blast load design procedure assumes a planar blast wave incoming from a detonation of a charge with mass W at a certain stand-off distance R from the structure to be designed. The Hopkinson–Cranz scaling law states that self-similar blast loads are generated by equal scaled distances Z [2], where Z is given by

$$Z = \frac{R}{\sqrt[3]{W}} \tag{1}$$

Experimental studies show that the cube root scaling law in (1) is valid across a large range of scaled distances, even as small as $Z = 0.32$ m/kg$^{1/3}$ [3]. Common practice is then to apply a time-dependent pressure $P(t)$ by the modified Friedlander equation [4, 5], i.e.,

$$P(t) = P_0 + P_r \left(1 - \frac{t - t_A}{t^+}\right) \cdot \exp\left(-b \cdot \frac{t - t_A}{t^+}\right) \quad (2)$$

onto the structure at hand, where P_0 is the ambient pressure, t_A is the shock wave time of arrival, P_r is the peak reflected overpressure generated by the blast wave, t^+ is the positive phase duration, and b is the decay coefficient. The quantities P_r, t^+, and b constitute the blast wave parameters and are determined based on experimental data like the seminal work by Kingery and Bulmash [6], which forms the basis for the "Conventional Weapons" (ConWep) programme [7].

So far, this pertains to idealised far-field planar blast waves, typically with moderate-to-large Z-values. At this point, it is useful to distinguish between a confined and a semi-confined environment. In the former case, the confinement causes a quasi-static pressure build-up after the initial shock has passed. If the volume in which the blast occurred is *completely* confined, i.e., there are no openings or exits for the pressure to escape, the quasi-static pressure will remain until an opening presents itself. In practice, engineering structures will have some kind of outlet (ventilation, windows shattered by the blast, open entries, etc.) that will eventually evacuate the pressure during and after the quasi-static build-up. Semi-confined environments add boundary conditions to blast, but large openings allow the pressure to escape more quickly (for instance, in open-ended tunnels or warehouses with large, open garage doors). It is this latter case which is the concern of this study.

Through increased pressure and impulse, the risk of injuries is elevated for confined and semi-confined blasts [8–10]. Further, a semi-confined environment may even amplify the damages caused by the negative phase [11]. Confinement effects account for the fact that much smaller contact charges are needed to breach a tubular concrete structure from the inside than from the outside [12]. Explosions inside tunnel-like geometries may even cause strong and long-lasting pressure oscillations [13]. The pressure histories of shock wave propagation may be very complex [14], and symmetries may cause multiple reflected shock waves to converge with strengths comparable to the initial shock [15]. Thus, internal detonations add several complicating factors: multiple reflections, interactions between waves, possible fluid–structure interaction (FSI) effects, openings, and irregular geometries to name a few.

In a confined space, the load is in typical engineering practice simplified into a bi-linear load containing the initial idealised shock pressure followed by an idealised gas pressure [5]. Other simplified approaches exist [16, 17], but to evaluate possible shadowing or amplification effects for which no test data are available, robust numerical models are crucial [18]. Naturally, numerical solutions are dependent on the discretisation [19]—finer discretisation gives, in general, more accurate solutions but adds to the computational time.

An alternative method is to use artificial neural networks for prediction of local structural response or prediction of blast parameters [20, 21]. Such methods do, however, ultimately depend on trustworthy training data for the neural network as Dennis et al. [20] also point out. It is in this space of generating trustworthy experimental and numerical data that the current study is placed.

Thus, in a combined experimental and numerical approach, the present work has two main goals: (i) to quantify internal, semi-confined blast loading by reliable and rigorous explosion tests and thereby establish a dependable experimental database and (ii) to use the experimental data for validation and verification of numerical models suitable for representing general blast loads with the intended application to structures. The experimental work consists of semi-confined detonations inside a rigid cylindrical environment using spherical composition C-4 charges of various sizes, and the results will through this work be made available to the research community for validation of any blast model. In short, the blast tests showed great repeatability, and the numerical results were able to accurately represent the experimental data.

2 Semi-confined blast experiments

2.1 Rig description and setup

Based on previous work on internal detonations [12], the pressure measurements in fragmenting concrete pipes were identified as uncertain because of the large displacements and rotations suffered by the concrete. Thus, new blast rigs were commissioned for the purpose of this study, which is to quantify internal, semi-confined blast loads and to compare them with numerical solutions. The rigs consist of thick-walled steel cylinders as shown in Fig. 1, with Kulite HKS-375 (M) pressure sensors mounted flush with the interior pipe wall. The sensors recorded with a frequency of 0.5 MHz.

Two different internal diameters D_i are used: 200 mm and 400 mm. The corresponding outer diameters are 250 mm and 500 mm. For each of the two diameters, three 1-m-long pipe sections were bolted together to form a 3-m-long tube as depicted in Fig. 1 and sketched in Fig. 2. Gaskets in milled grooves were used to make sure the connections were air-tight (two gaskets per connection). The explosive used was composition C-4 with an electrically ignited blasting cap, which adds approximately 2 g to the charge size. C-4 is designed to be a stable and self-contained explosive. Its high detonation velocity and low volatility leave little time or opportunity for any significant afterburning to occur in a semi-confined space where all the available oxygen has been used. The chemical composition of C-4 ensures that the

Fig. 1 Picture of blast test rig with $D_i = 400$ mm

Fig. 2 Sketch of blast rigs with $D_i = 200$ and 400 mm
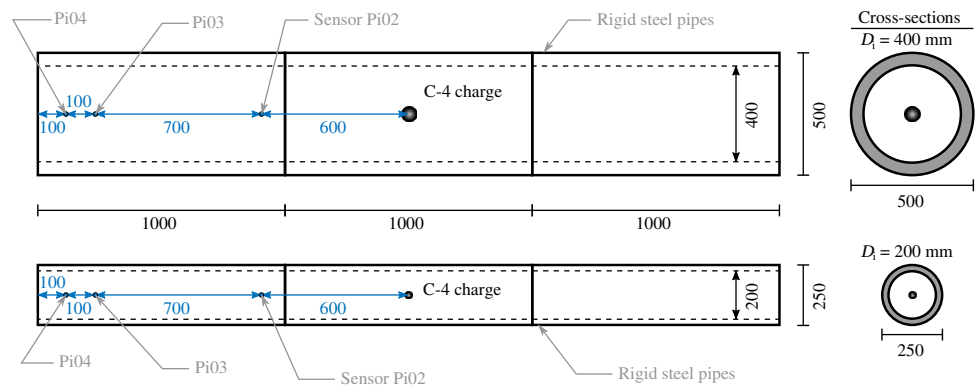
explosive reaction releases a large amount of energy in a short period of time, thus minimising the potential for any residual fuel to continue burning after the detonation due to oxygen limitations. Some instances of afterburning were noted, but at much later stages than the initial and reflected blast waves, which is the main concern of this study.

Since the charge shape has a notable effect for small values of Z [22, 23], all charges used herein were spherical. Thus, the chosen charge mass for each test relates to only one geometrical measure—the sphere radius. The detonator placement (inserted from the top to the centre of the charge) was kept constant in all tests as it might influence the results [24]. The charge was suspended in the centre of the pipe cross-section for all tests. Three pressure sensors were used to monitor the pressure, Pi02, Pi03, and Pi04, as laid out in Fig. 2. First, four repetitions of 20-g C-4 were conducted in the $D_i = 200$-mm rig. Next, two repetitions of multiple charge masses were performed in the $D_i = 400$-mm rig: 50, 65, 75, 100, 150, 200, 300, 400, and 500 g.

Finally, two repetitions of 10, 16, 20, and 25 g were carried out using the $D_i = 200$-mm rig with a slightly different sensor configuration—the longitudinal positions of the sensors (now called Pr01, Pr02, and Pr03) were 400 mm, 1200 mm, and 1300 mm instead of 600 mm, 1300 mm, and 1400 mm as shown in Fig. 3. This makes Pi03 in the first configuration identical to Pr03 in the second configuration. For this final series on the $D_i = 200$-mm rig, the exit of the pipe rig was filmed at 26,500 frames per second with a Phantom v2012

high-speed camera using shadowgraphy, enabling tracking of the exiting shock wave. Four additional sensors (P11 to P14) were used to measure the shock wave outside the rigid steel pipe as sketched in Fig. 3. Vertical pegs were added to indicate the sensor positions for the camera and to provide the pixel-to-mm conversion ratio. Sensors P11 to P14 were mounted on a plane steel table, which was flush-adjusted to the centre of the steel pipe wall.

2.2 Experimental results

An initial series of four repetitions of 20 g of C-4 was tested in the $D_i = 200$-mm pipe. The results in terms of pressure–time curves from sensors Pi02, Pi03, and Pi04 are plotted in Fig. 4, omitting test 3 due to irregularities in the test results. The tests show a high degree of repeatability, and the pressure magnitude is as expected between the sensors. Some local pressure peaks were noted on sensor Pi02 in Fig. 4, but the overall picture is one of consistent measurements.

A representative selection of data is plotted in Fig. 5 for the $D_i = 400$-mm pipe, using charge sizes of 150-g and 400-g C-4. (Pressure–time curves from the remaining charge sizes are given in the Appendix.) The tests show excellent repeatability. All tests are internally consistent with respect to the pressure measurements, and the rig behaved according to expectations. Primary, secondary, and even tertiary peaks were consistently reproduced for all charge sizes. In a flexible structure, an oscillating pressure like here and in

Fig. 3 Sketch of updated sensor configuration and camera view for blast rig with $D_i = 200$ mm
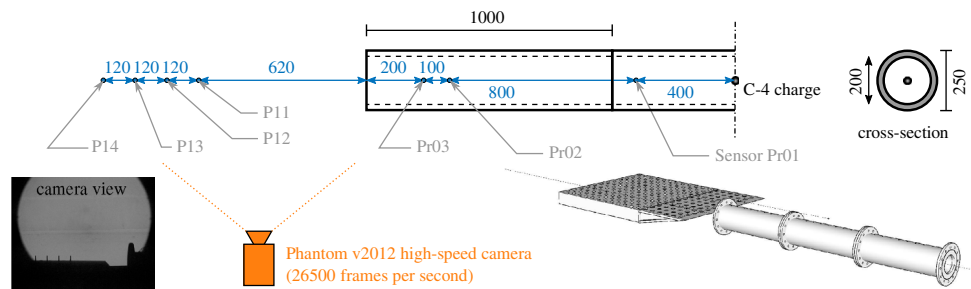

Fig. 4 Pressure–time curves from initial series of internal detonations of 20-g C-4 in $D_i = 200$-mm rigid steel pipe
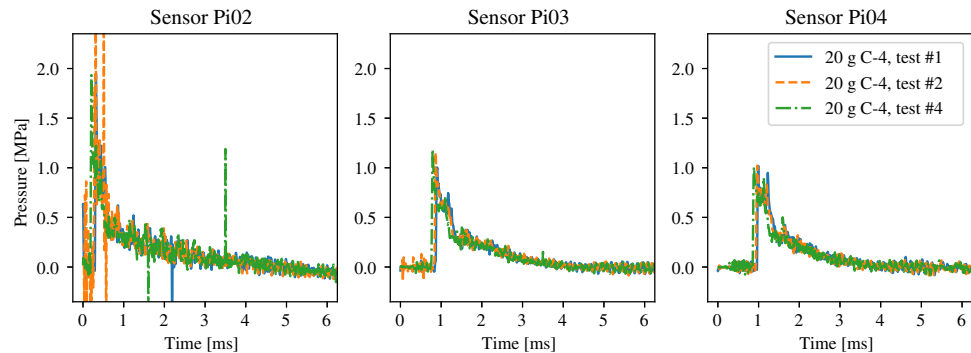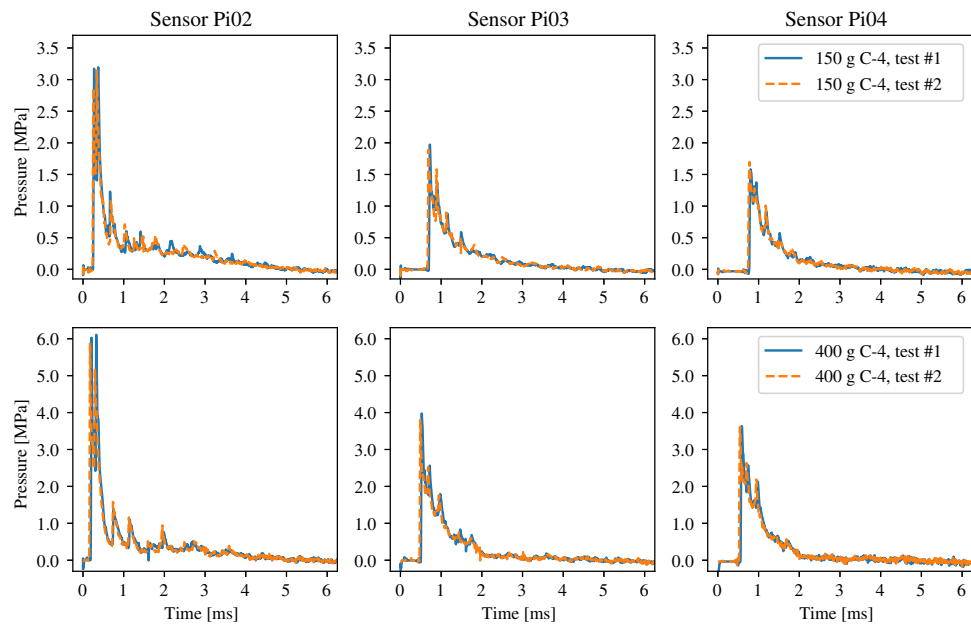

Fig. 5 Pressure–time curves from internal blast tests on $D_i = 400$-mm rigid steel pipe. The complete data set for all charges can be found in Figs. 24 and 25 in the Appendix

Ref. [13] may induce vibrations and motions—especially if the frequency of the recurring peaks harmonises with the structure's eigenfrequency.

The final set of detonations using 10, 16, 20, and 25 g of C-4 in the $D_i = 200$-mm rig using the sensor configuration from Fig. 3 also gave consistent and reproducible results. Further, the calibration was adjusted to lower the signal noise (compare Fig. 4 with Fig. 6). The first series in the $D_i = 200$-mm rig thus gave higher peak values for the pressure as seen in Table 1, while the impulses remained of similar magnitude as can be seen later from Tables 4 and 5. Unfortunately, there appeared to be a sensor malfunction for sensor Pr01 for the 20 and 25-g tests, which seemed to shift the pressure magnitude. The curves in the lower left part of Fig. 6 are thus not used for direct comparison but included for completeness. A repetition of all tests in Fig. 6 can be found in Fig. 26 in the Appendix, and the data may be downloaded from [25]. Peak pressure values from all sensors in all tests are listed in Table 1 along with relevant test parameters like the scaled distance to the pipe wall Z_{wall}.

Fig. 6 Internal pressure–time curves from internal detonations of 10, 16, 20, and 25-g C-4 in $D_i = 200$-mm pipe
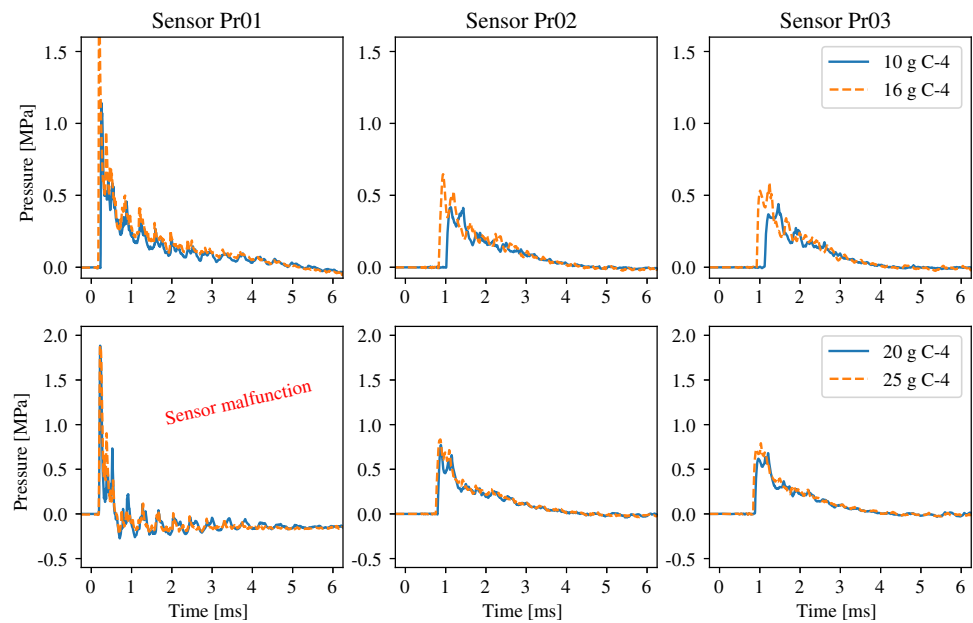
For the $D_i = 200$-mm tests using 10, 16, 20, and 25 g of C-4, four additional external sensors labelled P11–P14 were used along with a high-speed camera as sketched in Fig. 3. Thus, Fig. 7 juxtaposes the internal (left) and external (right) pressure recordings for the 16-g charge detonation in the $D_i = 200$-mm pipe. The pressure levels are one order of magnitude lower than the pressure recorded inside the tube because the shock wave is now able to expand in three dimensions. Further, the pressure approximately halves from sensor P11 to P14 (a distance of 360 mm). Figure 8 shows a time-lapse of the exiting shock wave using high-speed shadowgraphy, enabling a more qualitative comparison with numerical simulations. Image 1 shows the initial conditions, while images 2 and 3 show the shock wave just after exiting the rig. In these images, the shock wave is almost planar, while in the latter images it becomes spherical (see image 4 and on). Images 5, 6, 7, and 8 are the first images immediately after the shock wave passes sensors P11, P12, P13, and P14, respectively. The shadowgraphy images are in accordance with expectations for the various charge sizes and confirm the excellent repeatability of the tests. The complete set of pressure–time curves is included in the Appendix and is available for download [25] along with high-speed videos.

3 Numerical simulations of blasts in rigid steel pipes

Numerical simulations of the pipe blast experiments are performed by the EUROPLEXUS code [26]. EUROPLEXUS (abbreviated EPX) is a computer code jointly developed by the French Commissariat à l'Energie Atomique (CEA

DMT Saclay) and the Joint Research Centre of the European Commission (EC-JRC Ispra). The code application domain is the numerical simulation of fast transient phenomena such as explosions, crashes, and impacts in complex three-dimensional fluid–structure systems. The Cast3m [27] software from CEA is used as a pre-processor to EPX to generate the computational meshes.

3.1 Governing equations, discretisation, boundary conditions

The governing equations are the so-called Euler equations, where the fluid is considered compressible and inviscid. This is a particularisation of the Navier–Stokes equations, which express the conservation of mass, momentum, and energy. Viscous forces can be neglected in the present type of problem because they are very small compared with the pressure forces generated by the explosion.

The scope of these simulations is to calibrate the numerical model of the blast and to reproduce the experimental results from the pressure sensors on the pipe walls. The intended application is for internal blast load calculations of structures. Since the steel pipes in the tests have very thick walls and can be assumed as rigid, only the fluid domain is included in the numerical model. Figure 9 shows the Eulerian (fixed) mesh adopted. By exploiting the symmetries of the problem, only 1/8th of each pipe and air domain outside the pipe are represented in the numerical model.

Cell-centred finite volumes (CCFVs) are used for discretisation of the computational domain. Full second-order formulation both in space and in time is employed to achieve optimal accuracy in representing the shock waves produced

Table 1 Data from
semi-confined blast tests with
internal peak pressure
recordings from all sensors from
all tests sorted by charge size.
Note that only the Pr03/Pi03
sensors in the $D_i = 200$-mm
tests are directly comparable

D_i [mm]	W [g]	Rep. [–]	Z_{wall} [m/kg$^{1/3}$]	Peak pressure P_{peak} [kPa] at sensor no.				
				Pr01	Pr02/Pi02	Pr03/Pi03	Pi04	Data in
200	10	1	0.464	1068.1	426.4	402.0	–	Fig. 6
200	10	2	0.464	1142.4	417.7	439.5	–	Fig. 26
200	16	1	0.397	2063.5	602.7	540.3	–	Fig. 6
200	16	2	0.397	2121.1	646.5	588.9	–	Fig. 26
200	20	1*	0.368	–	1947.4	1001.8	1019.5	Fig. 4
200	20	2*	0.368	–	2565.1	1154.9	1021.0	Fig. 4
200	20	4*	0.368	–	1934.5	1184.4	1008.3	Fig. 4
200	20	1	0.368	1948.2[†]	753.7	626.3	–	Fig. 6
200	20	2	0.368	1884.2[†]	771.7	680.9	–	Fig. 26
200	25	1	0.342	1865.0[†]	853.5	804.5	–	Fig. 6
200	25	2	0.342	1881.7[†]	835.1	792.1	–	Fig. 26
400	50	1	0.543	–	2080.5	701.9	641.0	Fig. 24
400	50	2	0.543	–	1270.9	685.4	643.2	Fig. 25
400	65	1	0.497	–	1828.7	840.5	830.2	Fig. 24
400	65	2	0.497	–	1682.8	827.5	765.1	Fig. 25
400	75	1	0.474	–	2297.4	900.7	875.0	Fig. 24
400	75	2	0.474	–	1877.6	958.8	917.3	Fig. 25
400	100	1	0.431	–	3187.8	1151.4	1191.3	Fig. 24
400	100	2	0.431	–	2911.6	1239.4	1110.3	Fig. 25
400	150	1	0.376	–	3195.6	1972.2	1581.3	Fig. 5
400	150	2	0.376	–	3140.7	1891.4	1698.7	Fig. 5
400	200	1	0.342	–	3787.2	2770.9	2167.5	Fig. 24
400	200	2	0.342	–	4477.8	2716.4	2207.9	Fig. 25
400	300	1	0.299	–	4680.4	3024.3	2644.8	Fig. 24
400	300	2	0.299	–	6000.4	3421.6	2837.9	Fig. 25
400	400	1	0.271	–	6107.9	3975.2	3633.5	Fig. 5
400	400	2	0.271	–	5897.5	3799.1	3614.0	Fig. 5
400	500	1	0.252	–	6021.9	4873.8	4831.2	Fig. 24
400	500	2	0.252	–	6473.1	4794.5	4572.8	Fig. 25

*First series of $D_i = 200$-mm tests
[†]Sensor malfunction

Fig. 7 Results from detonation
of 16-g C-4 inside
$D_i = 200$-mm pipe showing the
pressure–time curves from
internal pressure sensors (left)
and external sensors (right). The
image numbers on the top
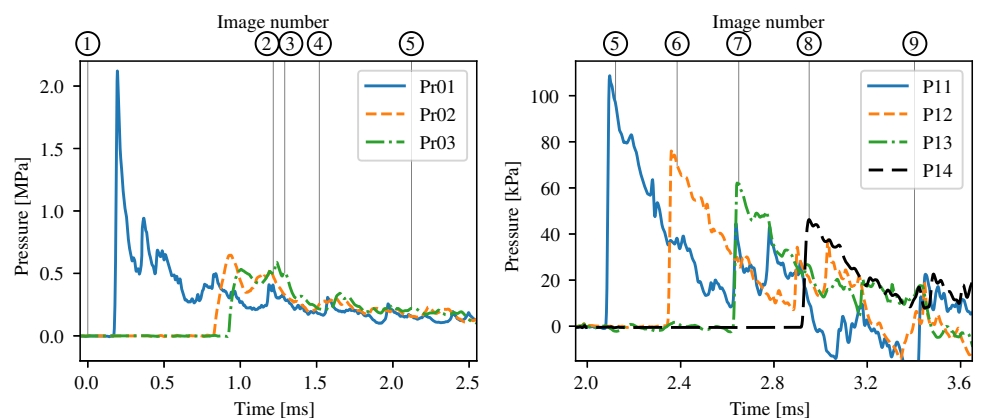abscissa refer to the high-speed
shadowgraphy images in Fig. 8

Fig. 8 Time-lapse of shadowgraphy images from 16-g charge detonated inside $D_i = 200$-mm rigid steel pipe. The time stamps indicate time after trigger initiation, and small vertical pegs have been added to indicate the sensor positions with measurements in mm
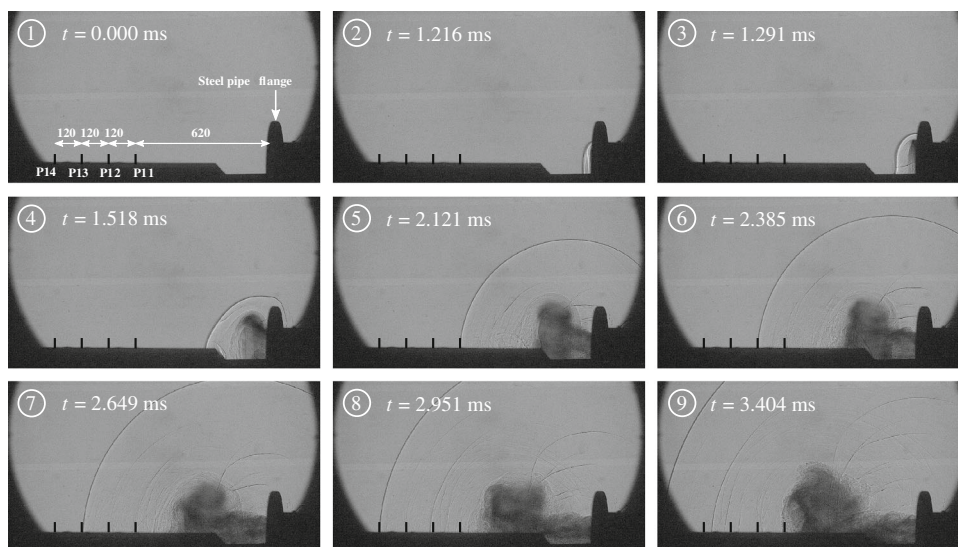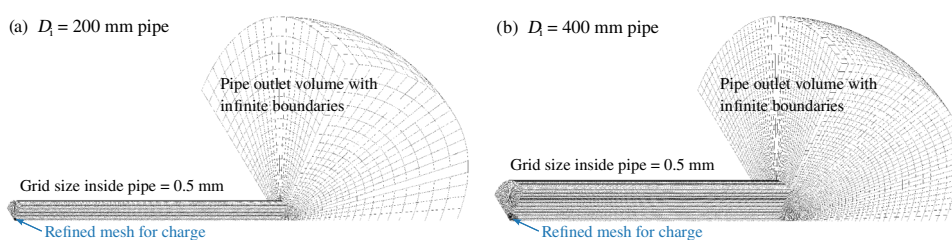
Fig. 9 Computational meshes (1/8th models) used in the simulations of rigid pipes. Confer Fig. 10 for details on the mesh in the charge area

by the detonation, in particular to capture the steep shock fronts, their multiple reflections and the narrow and steep pressure peaks and resulting impulses.

3.1.1 Fluid material model and modelling choices

In computational fluid mechanics, there are two alternative ways of solving the governing equations in a Eulerian formulation, namely by using either a single-component or a multi-component material model. In the EPX simulations presented here, the entire domain, i.e., both the explosive charge and the surrounding air, is modelled by the same constitutive equation, the well-known Jones–Wilkins–Lee (JWL) [28–30] equation of state (EoS). In EPX, this approach is realised via the JWLS material model (where the "S" is for solid), which consists of the JWL equation combined with the simple detonation model described in Sect. 3.1.4. It has the advantage (but also the limit) of allowing intermixing of the gaseous detonation products with the atmospheric air. The two fluids, namely the just-detonated C-4 products and the air, are considered to be the same fluid only at different initial states, i.e., different initial values of density, internal energy, and pressure. Technically, this means that a single-component material formulation is assumed in the Eulerian description of the problem. Each cell thus contains just one material component.

An alternative and more sophisticated approach (see, for instance, Rigby et al. [31], Alia and Souli [32]) consists in using a multi-component material formulation, whereby several (two, in this case) components with different EoSs may occupy the same computational cell. With this approach, the JWL EoS would be used (only) for the detonation products, while the air would typically be represented by the ideal gas EoS. Such formulations are more complex in that they require an interface-tracking algorithm, e.g., Young's VOF (volume-of-fluid) method [33] in the work by Alia and Souli [32]), to capture the interface between components within an element. Furthermore, numerical solution of the multi-component Euler equations requires a more involved technique (often referred to as operator splitting) than in the single-component case. As an example, see Ref. [32] for the stencil adopted in the work by Alia and Souli.

Thus, in the present approach both the initially solid charge and the surrounding atmospherical air are modelled by the JWL EoS [28–30]:

$$
\begin{aligned}
p =\ & A\left(1 - \frac{\omega}{R_1 V}\right) e^{-R_1 V} \\
& + B\left(1 - \frac{\omega}{R_2 V}\right) e^{-R_2 V} + \omega \rho i + \frac{\omega \lambda Q}{V}
\end{aligned}
\tag{3}
$$

Here, p is the absolute pressure, while A, B, R_1, R_2, and ω are material constants. Note that R_1, R_2, and ω are dimensionless

parameters, but A and B have the dimension of pressure. Next, i is the current internal energy per unit mass, and V (sometimes called the relative volume) is the current ratio

$$V = v/v_{\text{sol}} = \rho_{\text{sol}}/\rho \tag{4}$$

where v_{sol} and ρ_{sol} are the *initial* specific volume and density (both constant), respectively, of the solid explosive before detonation and v, ρ the *current* specific volume and density, respectively. Further, λ is the fraction of reacted detonation products leading to the afterburning pressure and Q is the afterburning energy release. As noted, no evidence of afterburning effects emerged from the tests, so the last term in (3) is thereby omitted in the simulations.

Once the solid explosive is exhausted, and after the expansion of the resulting combustion of gases, i.e., for large V, the two exponential terms in (3) (without the afterburning term) decay rapidly so that the pressure tends asymptotically towards the perfect-gas law, given by the following equation:

$$p = \omega\rho i = (\gamma - 1)\rho i \tag{5}$$

Thus, the parameter ω is related to the ratio γ between the specific heat capacities C_p and C_v at constant pressure and volume, respectively, of the gas by

$$\omega = \gamma - 1 = \frac{C_p}{C_v} - 1 \tag{6}$$

Several authors (see, for instance, Refs. [31, 32, 34]) adopt an expression of the asymptotic perfect-gas term of the JWL EoS (which, in a multi-component formulation, is used only for the detonation products and not for the air) which is apparently different from (5):

$$p = \omega \cdot \frac{E}{V} \tag{7}$$

with V being the relative volume from (4) and E is the internal energy per unit volume, with the dimensions of a pressure (J/m^3 or Pa). For the solid explosive and the just-detonated gas products, $E_{0,\text{C4}}$ (a constant, whose value can be found in the literature) is the chemical energy that may be released during the detonation process.

The two forms of the internal energy are related by

$$E = \rho i \tag{8}$$

which, particularised for the (undetonated) solid composition C-4 explosive, becomes

$$E_{0,\text{C4}} = \rho_{\text{sol}} i_{0,\text{C4}} = \rho_{0,\text{C4}} i_{0,\text{C4}} \tag{9}$$

where $\rho_{0,\text{C4}}$ is just an alternative notation for the solid density ρ_{sol}. Substituting (9) and (4) into (7) for the C-4 gives:

$$p = \omega\rho \cdot i_{0,\text{C4}} \tag{10}$$

which differs from (5) by the presence of $i_{0,\text{C4}}$ instead of i_{C4}. The two expressions become identical—and may thus be combined into a single EoS as in (3) valid for both components—if one assumes that the detonation products undergo an adiabatic transformation into the void (free adiabatic expansion). In an adiabatic, non-isentropic (irreversible) transformation, the specific internal energy remains constant ($i = i_0$). The adiabaticity of the expansion is justified by the extreme rapidity of the explosion. In addition, the expansion is (approximately) free since the resisting atmospheric pressure is very small compared with the pressure of the detonated gases, so that the work performed during the expansion is negligible.

The numerical values of the JWLS constants and of the other parameters assumed in the simulations are given in Table 2 and are mostly taken from the classical handbook by Dobratz and Crawford [34]. These are the values of the parameters most often used in the numerical simulations reported in the literature. The same values were also used by Rigby et al. [31] for their near-field in-air blast loading simulations with the LS-DYNA [35] code. Both the C-4 charge sizes and the distances involved in Rigby's simulations were comparable in magnitude with those of the present work.

3.1.2 Fluid boundary conditions

All fluid domain boundaries except the pipe outlet region are treated as rigid walls. This representation is well suited both for the internal wall of the pipe and for the symmetry planes. The fluid mesh is extended into a hemispherical region beyond the pipe outlet (illustrated in Fig. 9), and an infinite boundary condition at typical atmospheric values is prescribed on the spherical part of the boundary. This condition represents an infinite reservoir and is valid for perfect gases, such as (approximately) the mixture of air and expanded detonation products. According to the values of the speed normal to the interface $u_{n,\text{int}}$ and of the Mach number M_{int} (evaluated using the normal speed) inside the fluid domain, the following three cases are distinguished:

1. $M_{\text{int}} \leq 1$ corresponds to either a subsonic inlet ($u_{n,\text{int}} \leq 0$) or a subsonic outlet ($u_{n,\text{int}} > 0$). At the infinite boundary, a fictitious "ghost" cell is placed beyond the infinite boundary with prescribed values of pressure, density, and velocity (the latter typically being zero).
2. $M_{\text{int}} > 1$ and $u_{n,\text{int}} > 0$ represents a supersonic outlet. Then, as in the case of an absorbing boundary, the state

Table 2 Material constants for the JWLS material and other parameters for the simulations

Parameter	Description	Value	Units	References
A	Coefficient, C-4 and air	6.0977×10^{11}	Pa	[34]
B	Coefficient, C-4 and air	0.1295×10^{11}	Pa	[34]
R_1	Coefficient, C-4 and air	4.5	–	[34]
R_2	Coefficient, C-4 and air	1.4	–	[34]
ω_{C4}	Coefficient, C-4	0.25	–	[34]
ω_{air}	Coefficient, air	0.40	–	[31]
$E_{0,C4}$	Chemical energy, solid C-4	9.0000×10^9	$J/m^3 \equiv Pa$	[34]
$i_{0,C4} = E_{0,C4}/\rho_{sol}$	Initial internal energy, C-4	5.6215×10^6	J/kg	(9)
$i_{0,air} = p_{0,air}/(\omega_{air}\rho_{0,air})$	Initial internal energy, air	0.20686×10^6	J/kg	(5)
$\rho_{sol} \equiv \rho_{0,C4}$	Initial density, C-4	1601	kg/m^3	[34]
$\rho_{0,air}$	Initial density, air	1.225	kg/m^3	Measured
$p_{0,air}$	Atmospheric pressure, air	1.013×10^5	Pa	Measured
$\gamma_{C4} = \omega_{C4} + 1$	Heat capacity ratio, C-4	1.25	–	[34]
$\gamma_{air} = \omega_{air} + 1$	Heat capacity ratio, air	1.40	–	[31]
d	Speed of detonation front	8193	m/s	[34]

inside the fluid domain is copied outside into the ghost cell.

3. $M_{int} > 1$ and $u_{n,int} < 0$ indicates a supersonic inlet. This case cannot be treated and, if detected, produces a fatal error.

This formulation allows the high-pressure detonation waves to escape from the model without spurious reflections, causing the well-known "negative phase" of the blast pressure curve, whereby pressure falls below the atmospheric value. This permits fluid to re-enter into the model at later times, so that the atmospheric pressure is eventually recovered in the pipe.
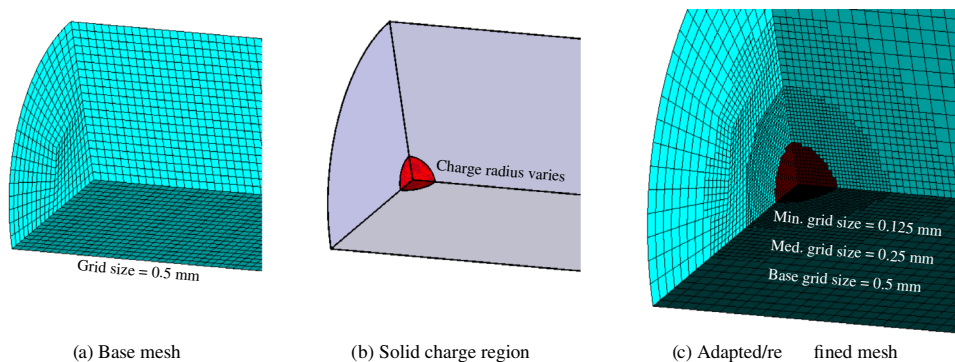
3.1.3 Fluid mesh

Figure 9 shows the computational meshes used for the 200-mm and 400-mm pipes. The solid charge region appears as a tiny darker zone at the centre of the (full) pipe, i.e., in the lower left corner of the 1/8th models. The total number of (base) fluid volumes (8-node hexahedra) including the mesh extensions beyond the pipe outlet is 90,700 for the small pipe and 386,000 for the large pipe. The main pipe region without the extension uses a grid of 300 volumes transversally times 266 volumes longitudinally (resulting in 79,800 volumes) for the small pipe, and 1200 volumes transversally times 263 longitudinally (315,600 volumes in total) for the large pipe, with a minimum size of the fluid mesh $h_F \approx 5$ mm.

3.1.4 Simple detonation model

A simple detonation model is employed. Detonation, i.e., the chemical reaction causing phase change from the solid explosive to the high-pressure gaseous detonation products, is assumed to start at the centre of the spherical solid charge. The detonation speed d is assumed constant and prescribed a value of $d = 8193$ m/s for the present model [34]. Each finite volume containing solid explosive detonates as soon as the detonation front reaches the centroid of the element. Then, the solid material in the element is suddenly replaced by the high-pressure gaseous products of detonation.

This modelling technique requires a very fine mesh in the solid charge region (the red zone in Fig. 10b), which in EPX is obtained by local adaptive refinement (see Fig. 10c) of the initial (or base) fluid mesh of Fig. 10a. During the simulation, once the charge has completely detonated so that all the material is in the gaseous state, and after the blast wave has propagated a certain distance, it is convenient to un-refine the fluid mesh in the charge region to reduce the CPU cost of the computation due to larger time steps, thus recovering the base mesh of Fig. 10a. As an example, Fig. 10 shows the computational mesh used for the 200-mm pipe with 22-g total charge, where a graded refinement up to level 3 (meaning two successive halvings of the mesh size) is used, so that the size of the refined fluid mesh becomes $h_F^{ref} = h_F/4 \approx 5/4 = 1.25$ mm. In all simulations, the fluid mesh was completely unrefined after $t_1 = 0.8$ ms.

Fig. 10 Computational mesh
details for the 200-mm rigid
pipe and 22-g total charge

(a) Base mesh   (b) Solid charge region   (c) Adapted/re   fined mesh

3.1.5 Mesh convergence

As mentioned, the base fluid mesh size is $h_F = 5$ mm as shown in Fig. 9. Simulations using 20 mm, 10 mm, and 4 mm were also run for comparison and to verify that a converging trend appears. The same mesh refinement technique for the charge was applied in all cases, and unrefined after 0.8 ms. The case with 400-g C-4 in $D_i = 400$ mm was chosen for the mesh convergence study. The results are shown in Fig. 11.

Pressures at positions equivalent to Pi02, Pi03, and Pi04 from Fig. 2 were extracted as a basis for comparison, and the corresponding impulse was obtained by integrating the pressure in time using the trapezoidal rule. Both the pressure (top row) and impulse (bottom row) are plotted in Fig. 11 for sensors Pi02, Pi03, and Pi04. As seen from the plots, the overall picture is very consistent across the different mesh sizes—even tertiary peaks and beyond are almost identical. Some differences in peak values for the pressure are noted in Table 3, as the coarser mesh tends to smooth out the pressure profiles. A more refined mesh thus gives higher peak values for the pressure, but these differences in pressure only amount to negligible differences in the impulses as shown in the bottom row of Fig. 11. Table 3 establishes a clear converging trend for the impulses despite the somewhat large peak pressure differences. At most, the peak pressure using $h_F = 20$ mm is almost 30% lower compared with using $h_F = 4$ mm for pressure sensor Pi04. We thus proceed with $h_F = 5$ mm, which had a reasonable computation time and should provide good visualisations of the shock wave.

3.2 Validation of the blast model

Two experimental data files were available for each nominal geometry (200 mm or 400 mm diameter) and charge mass. The scatter of results was low (apart from a few blatantly invalid recordings due to occasional sensor malfunction). The main comparisons will be performed in terms of pressure histories and impulses at the three sensors Pi02, Pi03, and Pi04 (or Pr01, Pr02, and Pr03 for the second series on the $D_i = 200$-mm pipe). The experimental data before the blast

wave arrives are cropped/zeroed, and the ambient pressure is subtracted. Additionally, the signal is shifted in time so that the pressure rises at the same time in the experiments as in the simulations for the *first* pressure sensor encountered.

For the sake of accuracy, time integration of the pressures to obtain the impulses is as mentioned performed with the trapezoidal rule by using all the available time values in the experimental and numerical signals. The time spacing of experimental signals from the data acquisition system was 2 µs, corresponding to 20,000 equispaced values over the 40 ms considered. On the simulation side, typical values of the automatic time integration step were about 0.1 µs in the detonation phase and 1 µs in the expansion phase. The chosen time spacing in the storage of numerical results was 1 µs over the first 5 ms of the simulation, and 10 µs thereafter, until the final time of 40 ms, for a total of 8501 values.

Comparing experimental and numerical impulses is preferable to directly comparing the overpressures because the impulse curves are smoother and, when one considers a structure subjected to the blast, the peaks and high-frequency oscillations of the overpressure are somewhat filtered out by the inertia of the structure (unless it is extremely thin and light), so that ultimately it is the impulse and not the overpressure alone, which is mainly felt by the structure and thereby determines its behaviour.

3.2.1 Illustration of a typical numerical simulation

Before showing the summarising comparisons, one case is presented in detail to illustrate the level of precision that can be obtained by the numerical simulation. The chosen test is the 400-mm pipe with 400 g of C-4 explosive plus 5 g of C-4 equivalent for the detonator. The experimental records can be found in Fig. 5 and the numerical records in Fig. 12. In general, the results for larger charges (like in this example) are in better agreement with the experiment, but also those for the smallest charges considered are still very good. For the small charges, the detonator is a large fraction (10–20%) of the total amount of explosive and is thereby important to get

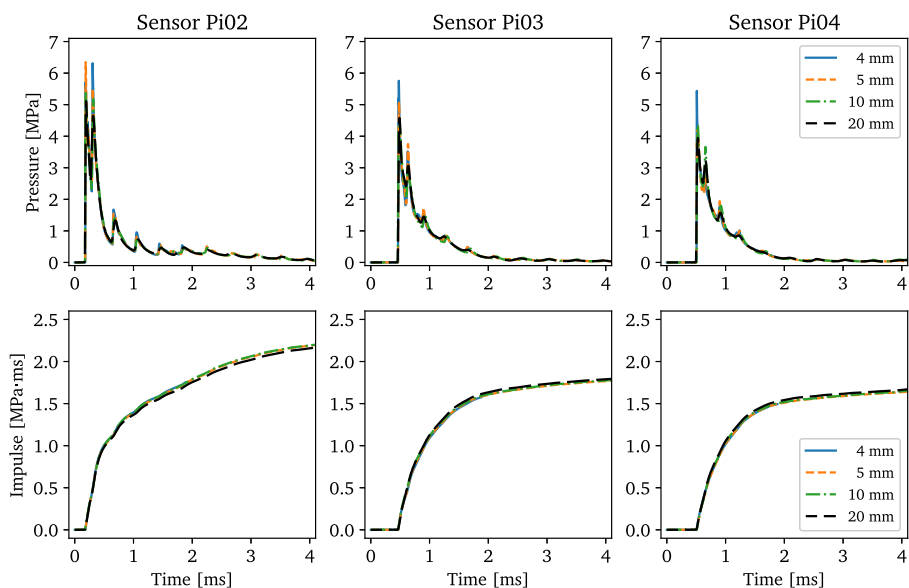**Fig. 11** Results in terms of pressure (top row) and impulse (bottom row) of the mesh convergence study

Table 3 Data from mesh convergence study where cell count and cell size refer to the base mesh without refinement

Cell count [–]	Cell size h_F [mm]	Peak pressure [kPa]			Impulse at 4 ms [kPa ms]		
		Pi02	Pi03	Pi04	Pi02	Pi03	Pi04
6275	20	5112	4578	3949	2158	1790	1663
48,700	10	5370	4468	4353	2193	1775	1647
386,000	5	6337	5405	4891	2196	1793	1640
752,500	4	6314	5757	5438	–*	–*	–*

*Simulation terminated prematurely at 1.88 ms

Fig. 12 Simulation results of absolute pressures computed in the 400-mm pipe with 405-g total charge
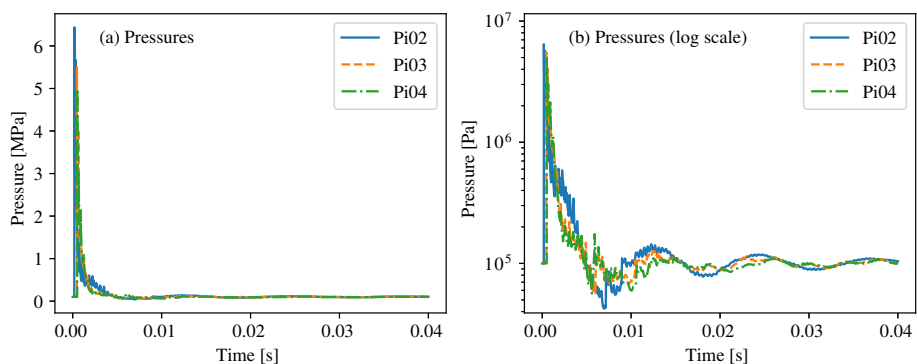
close to the true value, which is approximately equivalent to 2 g of C-4. For the larger charge sizes, the detonator is below 1% of the total charge.

Figure 12 shows the computed absolute pressures at the three sensors until 40 ms. All pressures converge precisely and smoothly to the atmospheric value at the end of the solution thanks to the infinite boundary condition, as can be appreciated in Fig. 12b where a logarithmic scale is used. The quality of this solution is confirmed by the pressure distributions, shown in Fig. 13, and by the velocity maps, shown in Fig. 14.

Figure 15 compares the corrected (without the ambient/atmospheric pressure) numerical overpressures and impulses (in orange) against the corresponding corrected experimental signals (black solid and black dotted curves, showing two tests) at the three sensors considered over the first 4 ms. The agreement, in particular of the impulses, is excellent. The experimental records are shifted in time so that the experimental and numerical signals (overpressure fronts) are synchronised at Pi02.

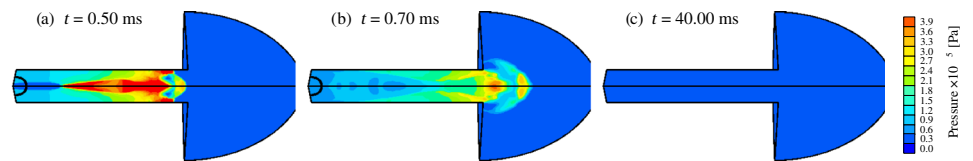**Fig. 13** Pressure maps in the 400-mm pipe with 405-g total charge

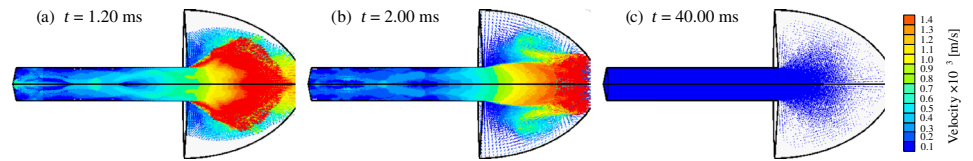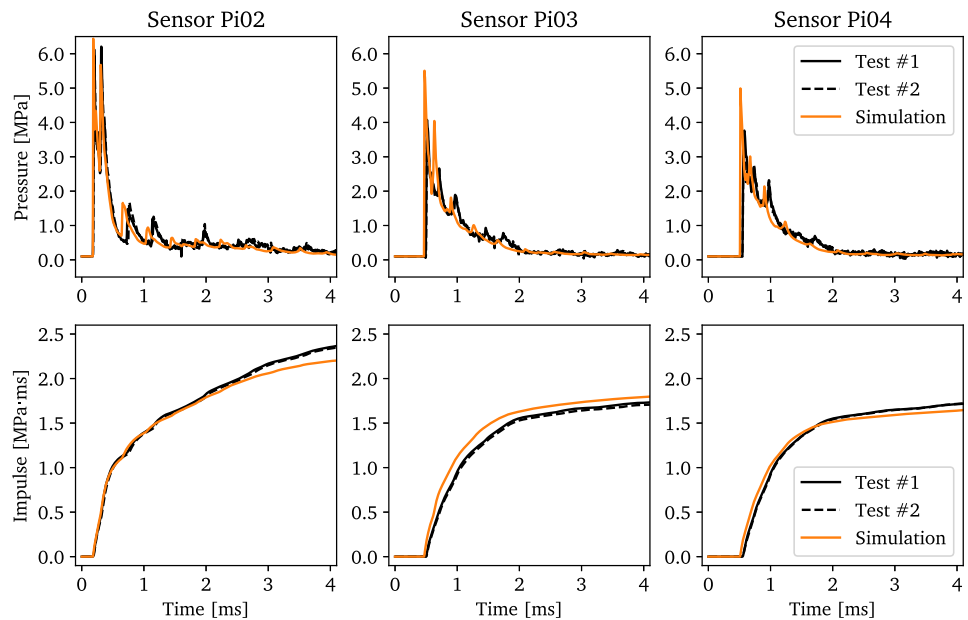**Fig. 14** Velocity maps in the 400-mm pipe with 405-g total charge

Fig. 15 Pressures and impulses in the 400-mm pipe with 405-g total charge compared with the experiments

3.2.2 Comparisons between experiments and simulations

The experimental and numerical impulses are now presented and compared for all test cases—see Fig. 16 for the 400-mm pipe and Fig. 17 for the 200-mm pipe. The agreement between experiment and simulation is as seen excellent for all the large pipe tests, while it is slightly less precise for the small pipe tests. This may be partly due to the fact that much smaller charges are used in the small pipe tests so that an even finer discretisation of the solid charge may be needed to achieve the same level of accuracy as for the large pipes. Besides, the charges are not perfectly spherical so the surface smoothness (or lack thereof) will have a larger influence on the smaller charges. It is also very difficult to physically place the charge exactly in the centre, both vertically and horizontally, and to place the detonator exactly in the centre of the charge. In any case, the accuracy looks largely sufficient for studies of the blast effects on structures. Beyond approximately 5 ms, most experimental signals show an evident

drift (typically, the atmospheric pressure value is not recovered exactly) and cannot be used to validate the numerical results beyond that time.

It should also be noted that all small pipe tests except one (the test with 20-g nominal charge, i.e., a total charge of 22 g including the detonator) were performed in a different series long after the first series of tests. As mentioned, some experimental records in this second series experienced sensor malfunction as indicated in the lower left of Fig. 6. Thus, the Pr01 readings for charge sizes 20 g and 25 g diverge in the lower left plot of Fig. 17. Another indication of possible small changes in the experimental conditions between the first and the second series of small pipe tests is the experiment with 20-g nominal charge (22 g including the detonator), which is the only one that had been performed also in the first series. The simulations are summarised in Tables 4 and 5 along with the corresponding experimental values for the peak pressure and the impulse after 4 ms.

Fig. 16 Comparison of impulses in the simulations (dashed curves) and experiments (solid curves) for all charge sizes used in the $D_i = 400$-mm pipe
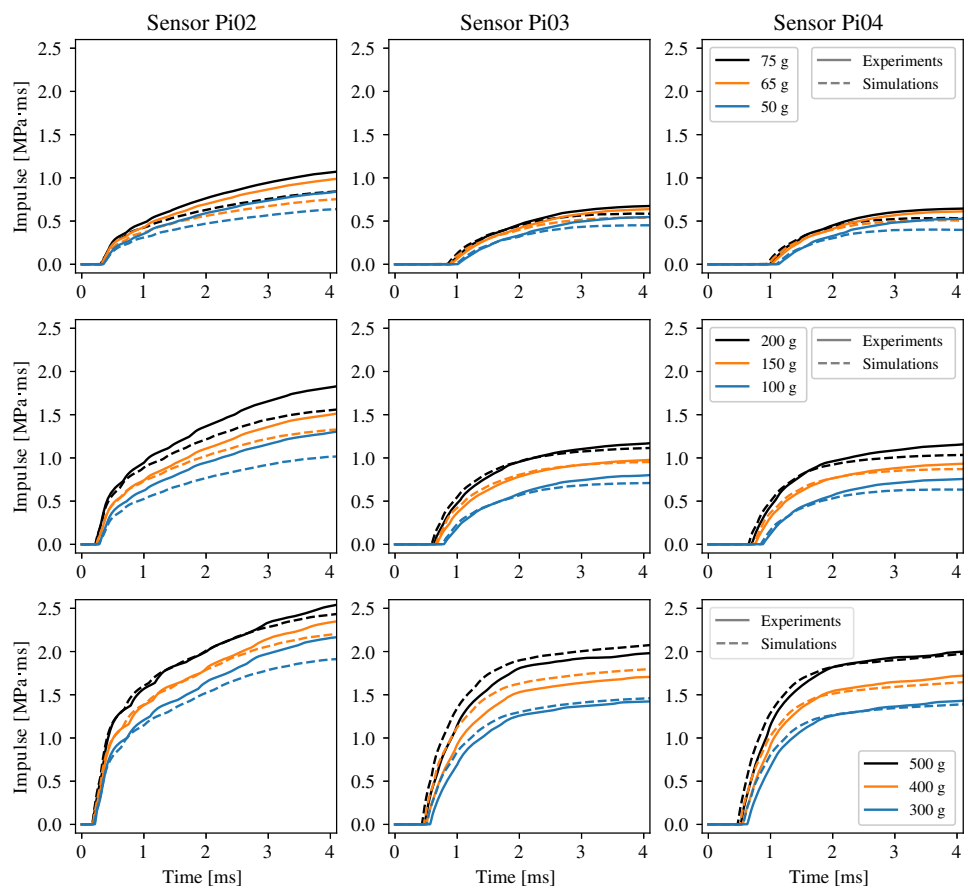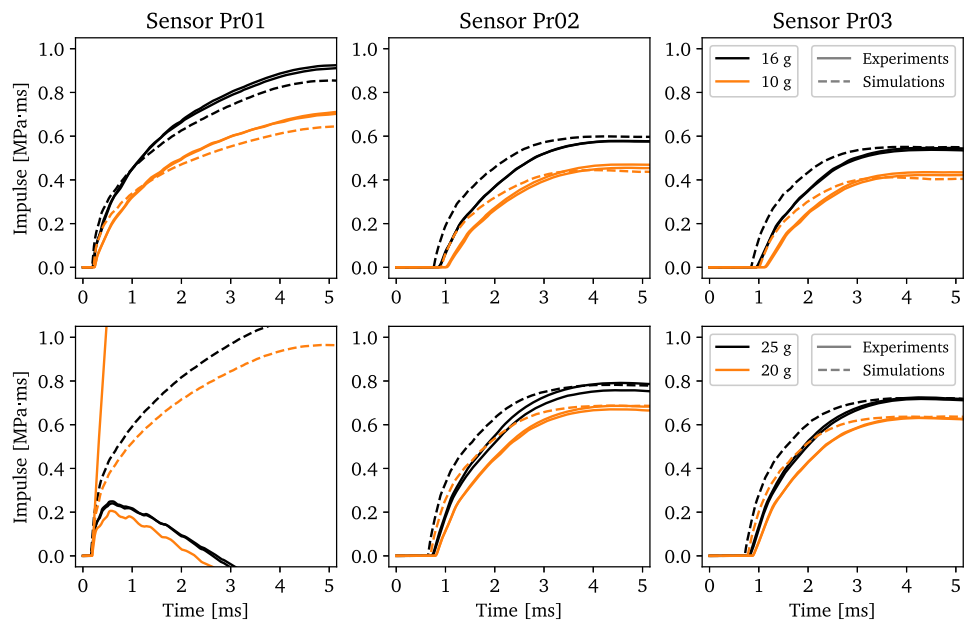

Fig. 17 Comparison of impulses in the simulations (dashed curves) and experiments (solid curves, two repetitions) for all charge sizes used in the $D_i = 200$-mm pipe. Sensor Pr01 suffered a malfunction for all the 20 and 25-g tests

3.2.3 Uncertainties affecting the pressure peaks

As it appears from the values reported in Tables 4 and 5, the agreement between the experimental and numerical impulses is generally better than that between the corresponding peak pressures. On the one hand, this is re-assuring, since the impulse is the most important quantity when studying the effects of an explosion on structures, except perhaps for

extremely light and thin structures. On the other hand, however, one might speculate about the reasons behind this result.

First of all, this result is not surprising, since the first pressure peak is very sharp and narrow in the detonations considered here. Therefore, the uncertainties in both its measurement and its numerical simulation are certainly considerably higher than those affecting the impulse. The relatively high variability (scatter) of the measured peak pressure in nominally identical experiments emerges also from the values of P_{peak} listed in Table 1.

On the experimental side, both the response time of the pressure transducers and the sampling frequency of the data acquisition must be adequate to precisely capture the peak. Further, the charge is not a perfect sphere and is not placed exactly in the centre of the pipe in any direction, whereas the simulations are perfectly symmetric. For the simulations, the results in terms of peak pressure (less for the impulse) are typically sensitive to parameters and details in the numerical model adopted. The time increment chosen automatically by the code is usually not of concern since, in explicit codes, it is already extremely small due to stability requirements of the numerical scheme.

Other characteristics of the simulation are more important in practice: for example, the order of the FV scheme both in space and in time, the solver for the calculation of numerical fluxes at interfaces between volumes (the so-called Riemann problem), and the flux limiter used in conjunction with higher-order schemes, among others. High-order schemes (such as the full second-order one used here) and "aggressive" solvers (such as the Harten, Lax, van Leer solver [36] used here, as improved by Toro and co-workers [37]) tend to deliver sharper and higher peaks, but may lead to numerical instabilities if pushed too far.

Without going into further details, which would bring us beyond the scope of the present paper, the best combination of model parameters were adopted in the code, as resulting from a long experience in this type of simulations. This ultimately produced a very good overall agreement with the experimental results, thus validating the model for application in engineering simulations of interest.

3.2.4 Choice of the time instant for impulse comparison

The main reason for comparing the experimental and numerical impulses at 4 ms in Tables 4 and 5 is that, at this instant, both results level out as shown in Figs. 15, 16 and 17 (the latter extending up to 5 ms), thus allowing for an easier comparison. The disagreement in impulse observed at the early stages could be almost completely eliminated by synchronising each numerical signal separately. However, using a

Table 4 Comparison of impulses after 4 ms (top half of table) and peak pressure data (bottom half) from numerical simulations (Num.) and physical tests (T1 and T2) using data from sensors Pi02, Pi03, and Pi04

Impulse at 4 ms from			Pi02 [kPa ms]			Pi03 [kPa ms]			Pi04 [kPa ms]		
	[mm]	[g]	Num.	T1	T2	Num.	T1	T2	Num.	T1	T2
PIPE91	200	20+2	866	898	938	633	664	672	554	628	633
PIPE92	400	50+3	635	842	830	453	557	545	402	537	525
PIPE93	400	65+3	748	998	980	540	637	635	509	607	610
PIPE94	400	75+3	839	1060	1063	587	673	672	536	644	643
PIPE95	400	100+3	1013	1271	1293	708	783	796	634	749	753
PIPE96	400	150+5	1324	1532	1501	953	960	972	871	912	928
PIPE97	400	200+5	1554	1807	1816	1112	1132	1164	1033	1114	1151
PIPE98	400	300+5	1908	2164	2158	1458	1436	1421	1386	1446	1427
PIPE99	400	400+5	2196	2354	2336	1793	1728	1703	1640	1712	1716
PIPE00	400	500+5	2425	2572	2525	2067	2024	1976	1967	2004	1994
Peak pressure from			Pi02 [kPa]			Pi03 [kPa]			Pi04 [kPa]		
PIPE91	200	20+2	2485	1947	1935	1321	1002	1184	1185	1020	1008
PIPE92	400	50+3	1141	2081	1271	671	702	685	686	641	643
PIPE93	400	65+3	1433	1829	1683	1018	841	828	1076	830	765
PIPE94	400	75+3	1759	2297	1878	1250	901	959	1125	875	917
PIPE95	400	100+3	1885	3188	2912	1286	1151	1239	1342	1191	1110
PIPE96	400	150+5	3187	3196	3141	2009	1972	1891	1623	1581	1699
PIPE97	400	200+5	3842	3787	4478	2632	2771	2716	2852	2168	2208
PIPE98	400	300+5	5062	4680	6000	3934	3024	3422	3511	2645	2838
PIPE99	400	400+5	6337	6108	5898	5405	3975	3799	4891	3634	3614
PIPE00	400	500+5	6987	6022	6473	5798	4874	4795	5431	4831	4573

Table 5 Comparison of impulses after 4 ms (top half of table) and peak pressure data (bottom half) from numerical simulations (Num.) and physical tests (T1 and T2) using data from sensors Pr01, Pr02, and Pr03

Impulse at 4 ms from			Pr01 [kPa ms]			Pr02 [kPa ms]			Pr03 [kPa ms]		
Case	D_i [mm]	C-4 [g]	Num.	T1	T2	Num.	T1	T2	Num.	T1	T2
PIPE131	200	10+2	612	666	662	445	463	448	410	433	420
PIPE132	200	16+2	824	871	887	599	603	646	550	535	544
PIPE162*	200	16+2	824	871	887	599	603	646	550	535	544
PIPE133	200	20+2	935	–	–	685	681	666	636	629	632
PIPE134	200	25+2	1067	–	–	781	784	752	722	722	716
Peak pressure from			Pr01 [kPa]			Pr02 [kPa]			Pr03 [kPa]		
Case	D_i [mm]	C-4 [g]	Num.	T1	T2	Num.	T1	T2	Num.	T1	T2
PIPE131	200	10+2	2724	1068	1142	915	426	418	706	402	440
PIPE132	200	16+2	3118	2064	2121	1246	603	647	1042	540	589
PIPE162*	200	16+2	3118	2064	2121	1246	540	589	1042	540	589
PIPE133	200	20+2	3126	–	–	1416	754	772	1302	626	681
PIPE134	200	25+2	3313	–	–	1703	854	835	1704	805	792

*Refined external mesh

different time-shift for different signals in the same simulation is not justifiable. Therefore, it is preferred to time-shift all numerical signals of a simulation by the same amount, namely the one needed to synchronise with the experiment the results at the sensor closest to the charge.

At times (much) larger than 4 ms, a few experimental impulses become unreliable because the measured pressures fail to asymptotically return exactly to the atmospheric value. This is contrary both to physical intuition and to the numerical results, in which the atmospheric value (zero over-pressure and thus steady impulse) is always exactly recovered towards the end of the simulation as seen in Fig. 12. For these reasons, the time instant at 4 ms is chosen for the comparisons.

3.2.5 Visualisation of the fluid flow

Figure 18 illustrates the complexity of the fluid flow in the small rigid pipe with a total charge of 22 g, as an example, by a schlieren-like representation, while Fig. 19 shows the large pipe with 155-g total charge. The grey levels indicate the magnitude of the density gradient (different in the two figures) and allow visualising the numerous reflections of the initially spherical blast wave on the pipe walls and along the pipe's main axis as the blast wave proceeds towards the open end of the pipe. All these phenomena become particularly evident and can, owing to the excellent fluid representation, be inspected in fine detail by playing the animations of the computational results. The lower half of each image includes the computational mesh. Note that the fluid mesh is unrefined in the initial charge region for $t > 0.8$ ms to reduce the CPU load.

A final model of the $D_i = 200$-mm pipe was made with a refined mesh for the external part (pipe162 in Table 5).

This allows a reasonable comparison with experiments using sensors P11–P14 sketched in Fig. 3. The 16-g charge test from Figs. 7 and 8 was chosen. Again, the numerical pressures and impulses match the experimental values decently as shown in Fig. 20. Schlieren-like images were produced by post-processing the numerical results for comparison with the shadowgraphy images exemplified by Fig. 8. The results are shown in Fig. 21, where the left column shows the shape of the shock wave emerging from the rigid steel pipe, and the right column shows the wave expanding into a sphere. The emerging shock wave has a rather flat front, which is rounded close to the edge of the rig. This shape eventually becomes spherical, and secondary peaks are noted inside the sphere. The numerical model captures these features excellently, creating confidence in the results from Figs. 18 and 19, which together with Fig. 21 provide a clear picture of both the internal and external wave propagations.

3.3 Influence of the heat capacity ratio γ for the air

While the single-component Eulerian formulation used in the EPX simulations has been shown to produce very good agreement with the experiments (in particular for the impulses), it has some approximations. The first approximation is that, at least in principle, one should use the same value of the ω parameter (and thus of γ, which is simply $\omega + 1$ as in (6)) for both the detonation products and the air. Yet, in the present simulations it has been assumed $\omega_{C4} = 0.25$, which is the value empirically calibrated by Dobratz and Crawford [34], and $\omega_{air} = 0.40$, which is the value used by Rigby et al. [31] in their multi-component simulations.

Then, each value of ω (or γ) is used over the entire simulation in the cells belonging to the corresponding initial spatial

Fig. 18 Schlieren representation of internal fluid flow in the small rigid pipe with 22-g total charge, where the legend on the right shows the spatial density gradient magnitude in (kg/m³)/m
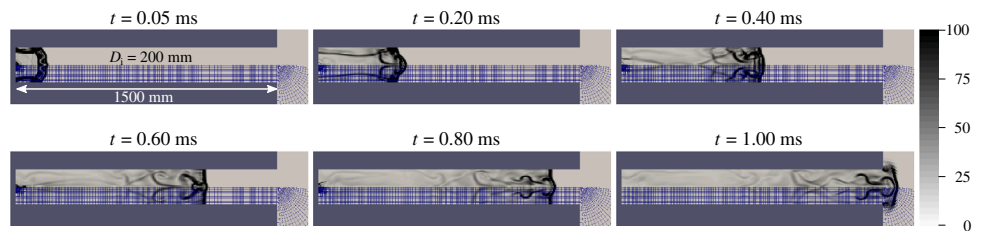

Fig. 19 Schlieren representation of internal fluid flow in the large rigid pipe with 155-g total charge, where the legend on the right shows the spatial density gradient magnitude in (kg/m³)/m
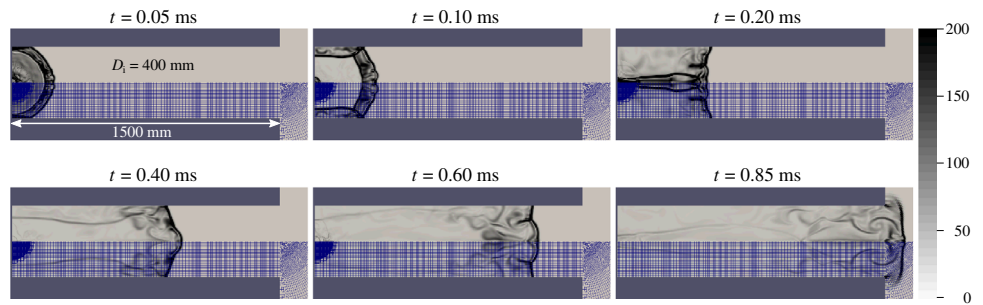

Fig. 20 Pressures (top row) and impulses (bottom row) outside the 200-mm pipe with (16+2)-g total charge simulations compared with the 16-g experiments
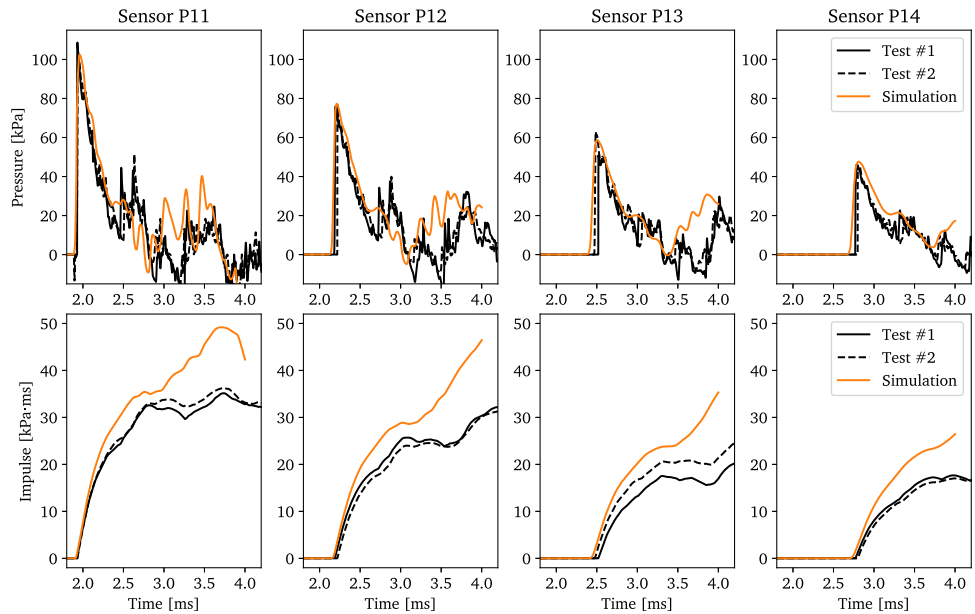
Table 6 Numerical simulations for the parametric study on γ for the air

Simulation	Diameter [mm]	Charge [g]	$i_{0,\text{C4}}$ [J/kg]	γ_{C4}	$i_{0,\text{air}}$ [J/kg]	γ_{air}
PIPE911	200	$20 + 2$	5.6215×10^6	1.25	0.20686×10^6	1.40
PIPE914	200	$20 + 2$	5.6215×10^6	1.25	0.33097×10^6	1.25
PIPE915	200	$20 + 2$	5.6215×10^6	1.25	0.25857×10^6	1.32
PIPE991	400	$400 + 5$	5.6215×10^6	1.25	0.20686×10^6	1.40
PIPE994	400	$400 + 5$	5.6215×10^6	1.25	0.33097×10^6	1.25
PIPE995	400	$400 + 5$	5.6215×10^6	1.25	0.25857×10^6	1.32

domain, i.e., $\omega = 0.25$ in the (tiny) region of the initial solid and $\omega = 0.40$ in the remaining region, initially occupied by the air. Consequently, when some detonation products pass from the initially solid domain to the initially pure air domain,

it is like their ω abruptly changes from 0.25 to 0.40, which is not realistic. However, since the extent of the solid region is extremely small compared with the entire fluid domain, the approximation introduced has limited effect on the results.

Fig. 21 Images showing the shock wave outside the rigid steel pipe rig with $D_i = 200$ mm, with the experiment in the top row and the simulation in the bottom row. The white arrows indicate approximately the internal radius of 100 mm for the pipe
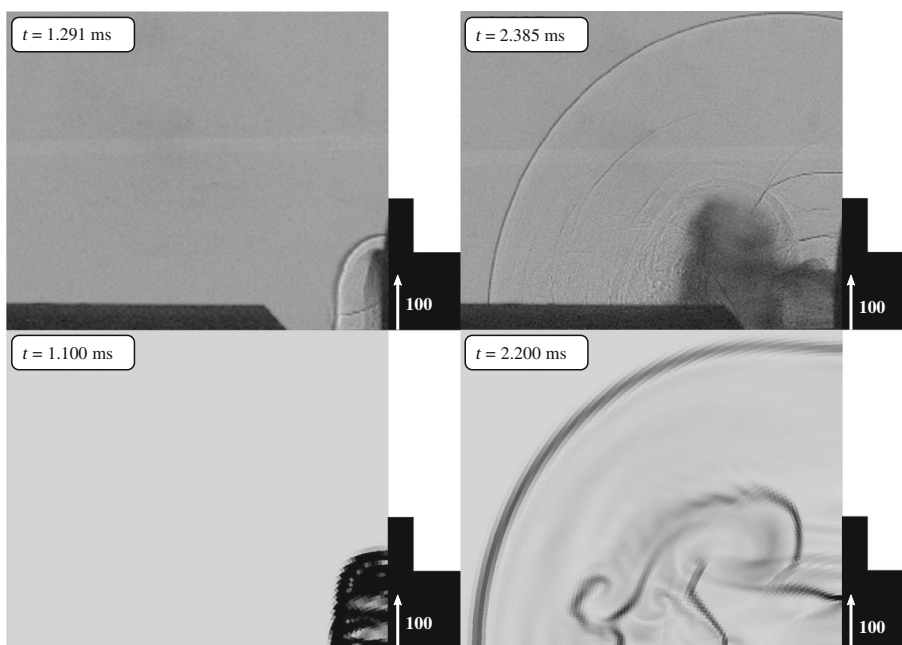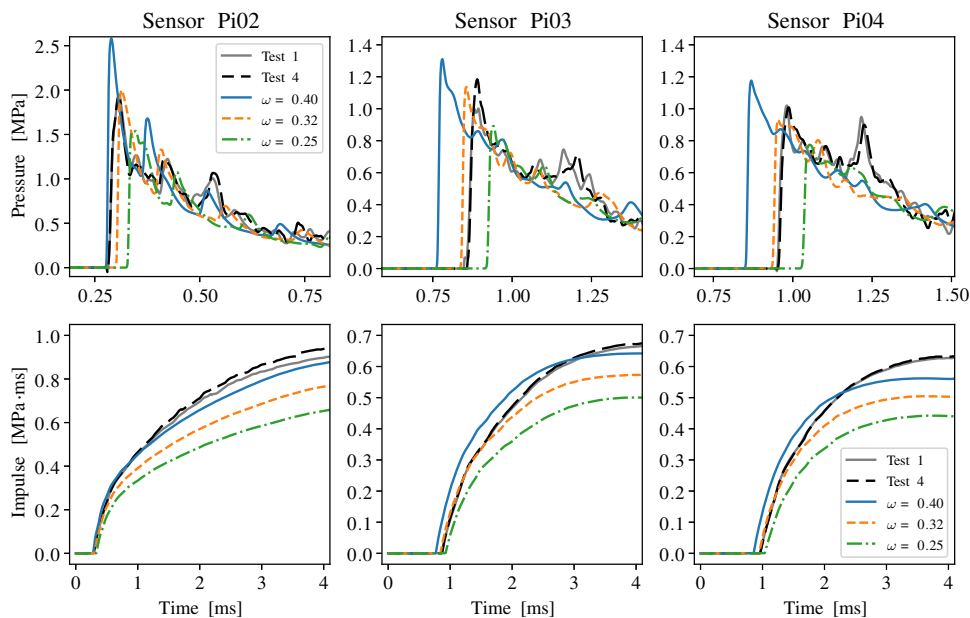

Fig. 22 Comparison of results for the 200-mm case with $(20+2)$-g C-4 by varying ω_{air}

A second and more important approximation concerns the use of a constant value of ω in the model. While this is correct for the C-4 material, as assumed in [34], it is certainly just an approximation for the air. The value of γ_{air} decreases with increasing temperatures, passing from 1.40 at room temperature (20 °C) to about 1.32 for temperatures of the order of those occurring during the blast (hundreds of °C), ultimately tending asymptotically to 1.

Additional simulations were thereby performed by keeping a constant $\gamma_{C4} = \omega_{C4} + 1 = 1.25$ and by varying the γ_{air} values among 1.40, 1.32, and 1.25. The exercise was done for the 200-mm pipe with a $(20 + 2)$-g charge and for

the 400-mm pipe with a $(400 + 5)$-g charge. These simulations are listed in Table 6. As γ_{air} is varied, $i_{0,air}$ is modified accordingly in order to obtain the experimentally measured atmospheric pressure $p_{0,air} = 1.013 \times 10^5$ Pa via (5).

The results are presented in Figs. 22 and 23, where the time scale is narrowed to clearly discern the pressure peaks. Note that the impulse values are presented over the usual time window up to 4.0 ms.

It can be seen that the value of γ affects the height of the pressure peaks and their timing, but also the impulses. By decreasing the value of γ, the maximum overpressure decreases, the shock front becomes slower and the impulse

Fig. 23 Comparison of results
for the 400-mm case with
(400+5)-g C-4 by varying γ_{air}
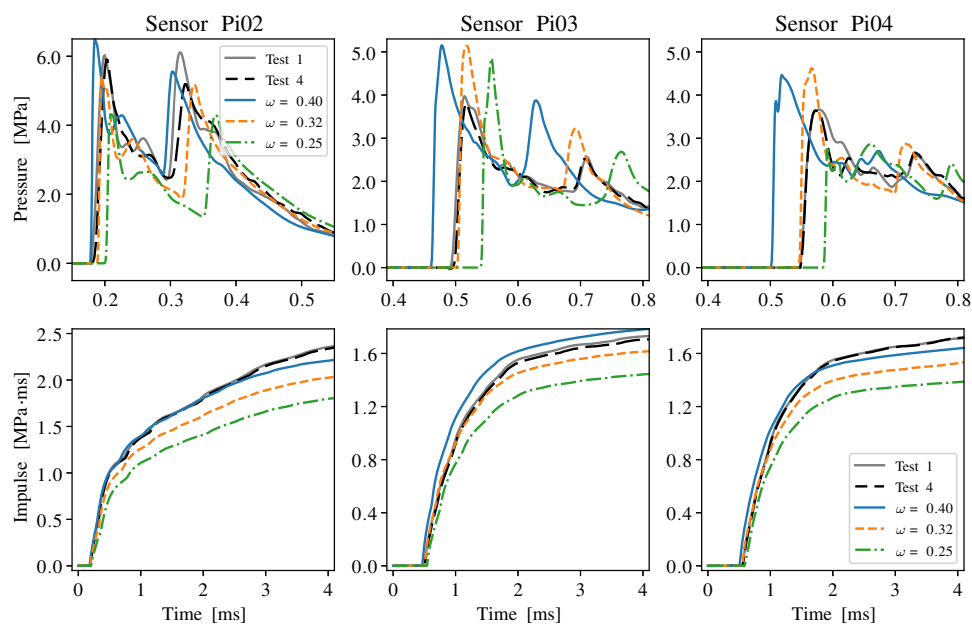
decreases. The value of γ, which best fits the experimental
pressure curve with respect to peaks and timing, is $\gamma = 1.32$,
which is the value expected for air at high temperature. How-
ever, the impulses with $\gamma = 1.32$ are underestimated and the
best fit of impulses is obtained for $\gamma = 1.40$. This justi-
fies the choice of $\gamma_{air} = 1.40$ adopted for the simulations
described in the previous sections where the intended appli-
cation is to structures subjected to internal blast loading, e.g.,
a submerged floating tube bridge [38].

Although the overall agreement obtained in this work
is already very good, there is of course always room for
improvement. Future work in this respect will concentrate on
the two most important aspects, which have emerged from
the current study. First, the validation and use of a multi-
component detonation model, dubbed the JWLR material
model, which is in an advanced development stage within
EPX. Second, the implementation of a variable γ as a func-
tion of the temperature in the perfect-gas law (not in the JWL
law) to be used for the air component in the JWLR model.

4 Concluding remarks

This study set out to achieve two main goals: (i) to establish
a reliable experimental database for internal blast loads and
(ii) to validate a numerical approach for the internal blast
loads. The blast tests carried out inside the rigid steel pipes
showed great repeatability across a wide range of charge
sizes. Two internal diameters were used for the steel pipes,
increasing the experimental range. Shadowgraphy videos
showing the shock wave exiting the smaller pipe showed
an almost planar shock wave directly after exit, then tran-

sitioning into a spherical wave. All pressure recordings
were internally consistent and highly repeatable, which is
not granted when dealing with high explosives. Apart from
a few sensor malfunctions—which are difficult to avoid
completely—all tests were successful and contributed to
achieving the first goal.

Concerning the second goal, it has been shown that
with modern finite volume-based fluid models and advanced
numerical techniques such as dynamic fluid mesh adap-
tivity, it is possible to simulate the effects of blasts in
rigid cylindrical pipes with a high degree of accuracy. The
obtained fluid models, validated against well-instrumented
and highly-reproducible experimental tests, were able to
decently capture pressure peaks from secondary and even ter-
tiary reflections, resulting in nicely matching impulse curves.
Comparisons with the shadowgraphy images showed that the
shock wave shapes were accurately captured qualitatively as
well. Thus, the numerical results were in excellent agreement
with the experimental data both quantitatively and quali-
tatively, inside the pipe and outside, as illustrated by, for
instance, Figs. 16 and 21. The accuracy of numerical results
is contingent upon modelling strategies and assignment of
model parameters. By varying the heat capacity ratio γ for
the air, it was shown that it is possible to capture the pres-
sure peaks and the timing better, albeit at the expense of the
impulse accuracy. The choices herein were made on the basis
of representing the impulse most accurately for the intended
purpose of application to engineering structures.

The validated fluid model can thus be used to simulate
the much more difficult case whereby the pipe is deformable
and made of a complex structural material such as plain or
reinforced concrete [12]. While simplified approaches like

ConWep can provide decent first-order approximations [38], preliminary work has shown that it is essential to include fluid–structure interaction to capture the cracking and fragmentation of the concrete pipe [39]. Full fluid–structure interaction allows the large deformation and failure of the structure to affect the load and vice versa [40]. The complex pressure histories and wave patterns observed show that an accurate fluid representation is indispensable for this type of load. Further, a material test-based calibration is needed for the concrete constitutive relation for accurate results [41], but this is out of scope for the current study and thereby left for future investigations.

Appendix: Pressure recordings from blast experiments

This appendix includes the pressure–time curves from all detonation experiments carried out inside the rigid steel cylinders for both $D_i = 200$ mm and 400 mm and all charge sizes (ranging from 10 to 500 g). The complete data set of pressure recordings from Sect. 2 is included in this appendix for completeness. Text files with the raw data, along with high-speed videos, are available for download from Ref. [25] (Figs. 24, 25, 26, 27, 28).

Fig. 24 Pressure–time curves from first repetition on $D_i = 400$-mm rigid steel pipe tests
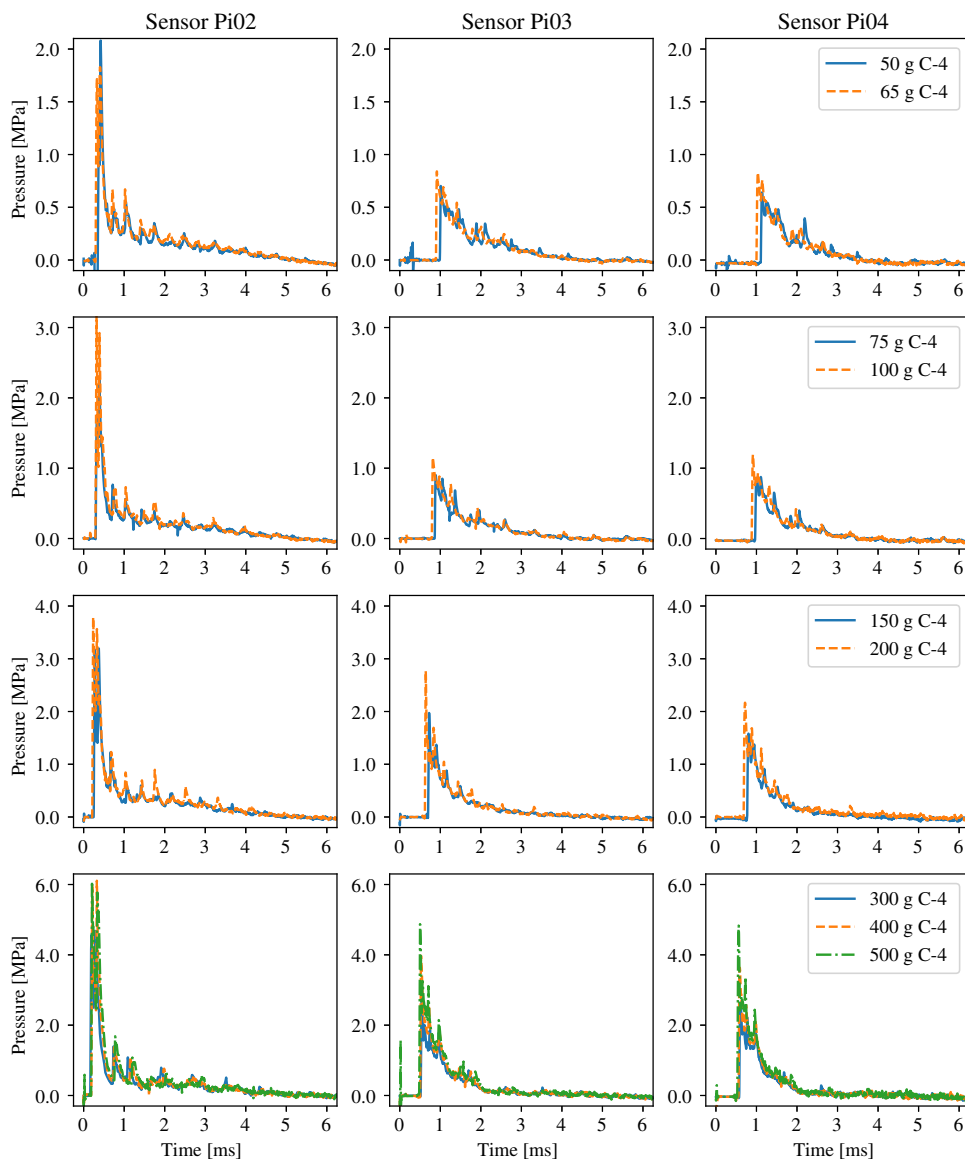
Fig. 25 Pressure–time curves from second repetition on $D_i = 400$-mm rigid steel pipe tests
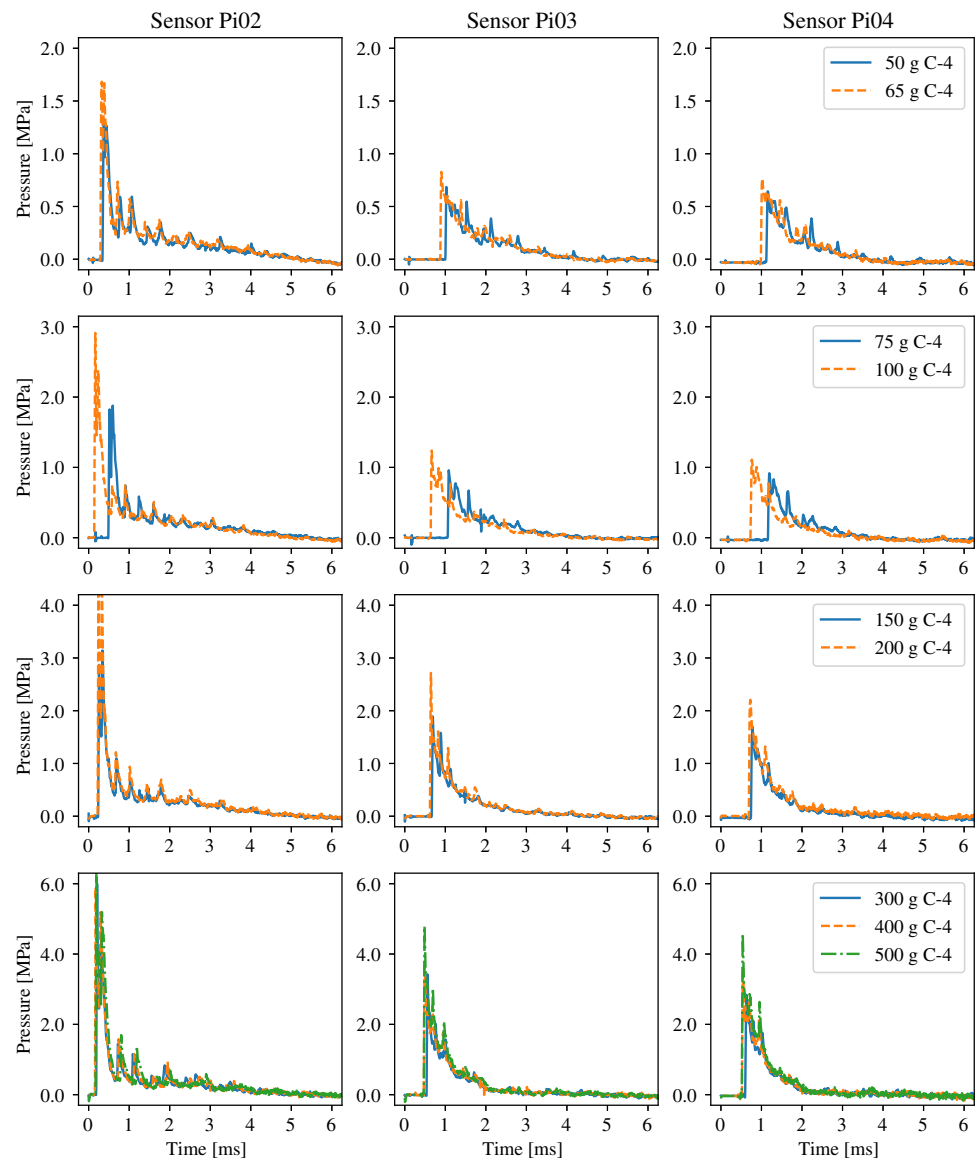
Fig. 26 Internal pressure–time curves from second repetition of internal detonations of 10, 16, 20, and 25-g C-4 in $D_i = 200$-mm rigid steel pipe
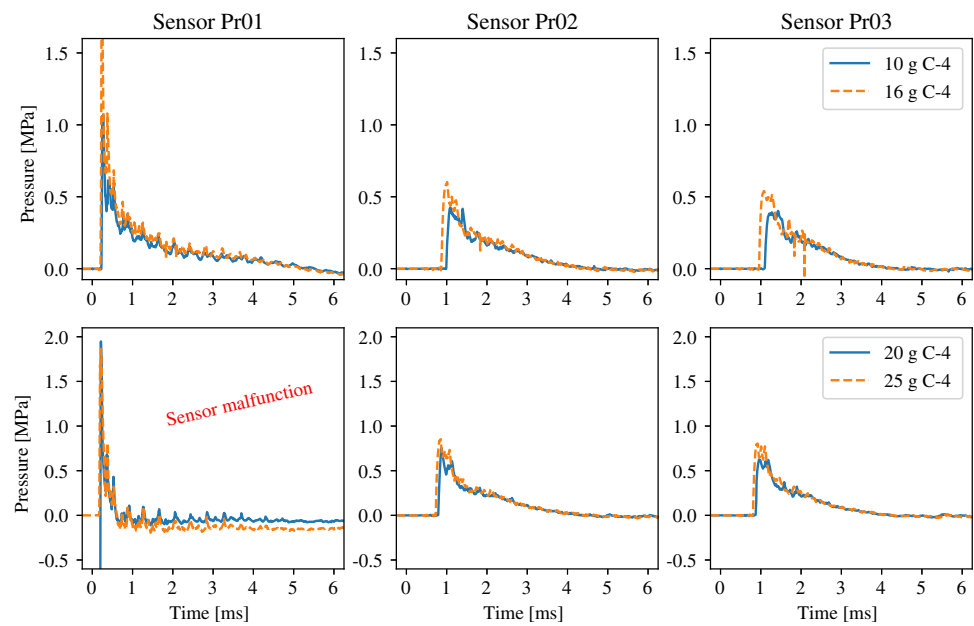
Fig. 27 External pressure–time curves from first repetition of internal detonations of 10, 16, 20, and 25-g C-4 in $D_i = 200$-mm rigid steel pipe
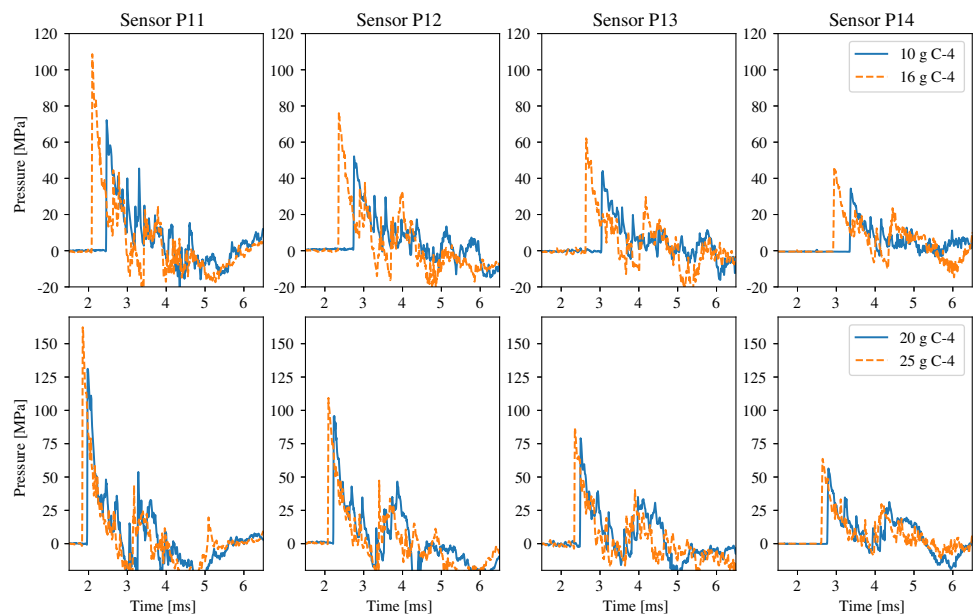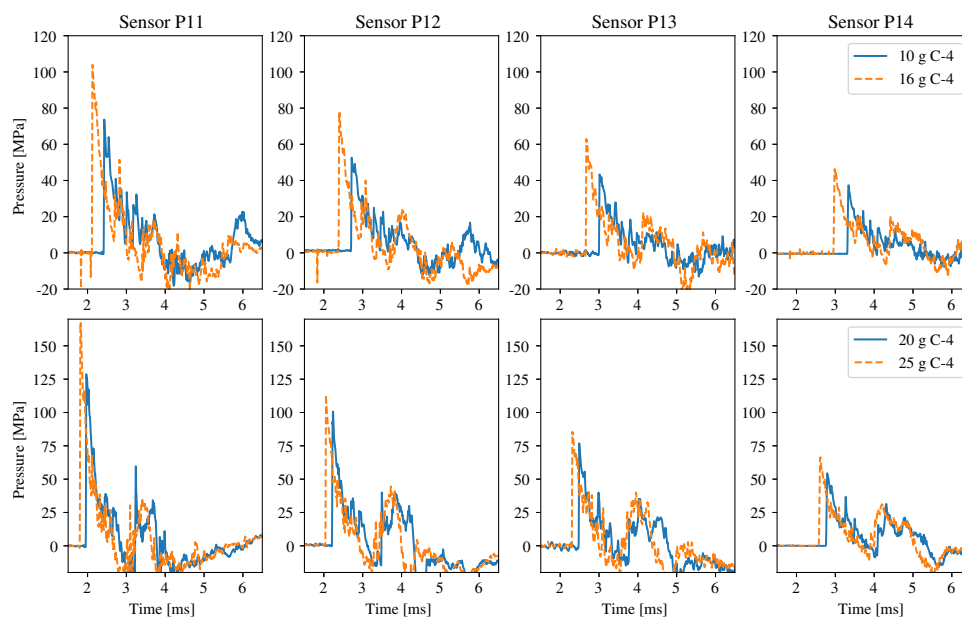
Fig. 28 External pressure–time curves from second repetition of internal detonations of 10, 16, 20, and 25-g C-4 in $D_i = 200$-mm rigid steel pipe

Declarations

Conflict of interest The authors declare that no personal or financial interest has had any influence on the research carried out herein. No organisations or individuals are expected to experience any monetary gain or loss as a result of publishing this work.

References

1. European Union: Directive (EU) 2022/2557 on the resilience of critical entities. Off. J. Eur. Union **L333**, 164 (2022). http://data.europa.eu/eli/dir/2022/2557/oj

2. Conrath, E.J., Krauthammer, T., Marchand, K.A., Mlakar, P.F.: Structural Design for Physical Security: State of the Practice. American Society of Civil Engineers, New York (1999). https://doi.org/10.1061/9780784415498

3. Esparza, E.D.: Blast measurements and equivalency for spherical charges at small scaled distances. Int. J. Impact Eng. **4**(1), 23–40 (1986). https://doi.org/10.1016/0734-743X(86)90025-4

4. Friedlander, F.G.: The diffraction of sound pulses I: diffraction by a semi-infinite plane. Proc. R. Soc. A: Math. Phys. Eng. Sci. **186**(1006), 322–344 (1946). https://doi.org/10.1098/rspa.1946.0046

5. Krauthammer, T.: Modern Protective Structures. CRC Press, Boca Raton (2008)

6. Kingery, C.N., Bulmash, G.: Airblast parameters from TNT spherical air burst and hemispherical surface burst. Technical report, Defence Technical Information Center, Ballsitic Research Laboratory, Aberdeen Proving Ground, MD (1984)

7. Conventional Weapons Effects Program. Vicksburg: Department of the Army. Waterways Experiment Station, Corps of Engineers (1993)

8. Langenderfer, M., Williams, K., Douglas, A., Rutter, B., Johnson, C.E.: An evaluation of measured and predicted air blast parameters from partially confined blast waves. Shock Waves **31**, 175–192 (2021). https://doi.org/10.1007/s00193-021-00993-0

9. Rezaei, A., Salimi Jazi, M., Karami, G.: Computational modeling of human head under blast in confined and open spaces: primary blast injury. Int. J. Numer. Methods Biomed. Eng. **30**(1), 69–82 (2014). https://doi.org/10.1002/cnm.2590

10. Valsamos, G., Casadei, F., Solomos, G., Larcher, M.: Risk assessment of blast events in a transport infrastructure by fluid–structure interaction analysis. Saf. Sci. **118**, 887–897 (2019). https://doi.org/10.1016/j.ssci.2019.06.014

11. Sauvan, P.E., Sochet, I., Trélat, S.: Analysis of reflected blast wave pressure profiles in a confined room. Shock Waves **22**, 253–264 (2012). https://doi.org/10.1007/s00193-012-0363-1

12. Kristoffersen, M., Hauge, K.O., Minoretti, A., Børvik, T.: Experimental and numerical studies of tubular concrete structures subjected to blast loading. Eng. Struct. **233**, 111543 (2021). https://doi.org/10.1016/j.engstruct.2020.111543

13. Bratland, M., Bjerketvedt, D., Vaagsaether, K.: Structural response analysis of explosions in hydrogen–air mixtures in tunnel-like

geometries. Eng. Struct. **231**, 111844 (2021). https://doi.org/10.1016/j.engstruct.2020.111844

14. Julien, B., Sochet, I., Vaillant, T.: Impact of the volume of rooms on shock wave propagation within a multi-chamber system. Shock Waves **26**, 87–108 (2016). https://doi.org/10.1007/s00193-015-0603-2

15. Chan, P.C., Klein, H.H.: A study of blast effects inside an enclosure. J. Fluids Eng. **116**(3), 450–455 (1994). https://doi.org/10.1115/1.2910297

16. Dragos, J., Wu, C., Oehlers, D.J.: Simplification of fully confined blasts for structural response analysis. Eng. Struct. **56**, 312–326 (2013). https://doi.org/10.1016/j.engstruct.2013.05.018

17. Edri, I.E., Grisaro, H.Y., Yankelevsky, D.Z.: TNT equivalency in an internal explosion event. J. Hazard. Mater. **374**, 248–257 (2019). https://doi.org/10.1016/j.jhazmat.2019.04.043

18. Remennikov, A.M., Rose, T.A.: Modelling blast loads on buildings in complex city geometries. Comput. Struct. **83**(27), 2197–2205 (2005). https://doi.org/10.1016/j.compstruc.2005.04.003

19. Caçoilo, A., Teixeira-Dias, F., Mourão, R., Belkassem, B., Vantomme, J., Lecompte, D.: Blast wave propagation in survival shelters: experimental analysis and numerical modelling. Shock Waves **28**, 1169–1183 (2018). https://doi.org/10.1007/s00193-018-0858-5

20. Dennis, A.A., Pannell, J.J., Smyl, D.J., Rigby, S.E.: Prediction of blast loading in an internal environment using artificial neural networks. Int. J. Protect. Struct. **12**(3), 287–314 (2021). https://doi.org/10.1177/2041419620970570

21. Dennis, A.A., Rigby, S.E.: The direction-encoded neural network: a machine learning approach to rapidly predict blast loading in obstructed environments. Int. J. Protect. Struct. (2023). https://doi.org/10.1177/20414196231177364

22. Rushton, N., Schleyer, G.K., Clayton, A.M., Thompson, S.: Internal explosive loading of steel pipes. Thin-Walled Struct. **46**(7), 870–877 (2008). https://doi.org/10.1016/j.tws.2008.01.027

23. Shi, Y., Wang, N., Cui, J., Li, C., Zhang, X.: Experimental and numerical investigation of charge shape effect on blast load induced by near-field explosions. Process Saf. Environ. Prot. **165**, 266–277 (2022). https://doi.org/10.1016/j.psep.2022.07.018

24. Needham, C., Brisby, J., Ortley, D.: Blast wave modification by detonator placement. Shock Waves **30**, 615–627 (2020). https://doi.org/10.1007/s00193-020-00958-9

25. Kristoffersen, M., Hauge, K.O.: Pressure measurements from internal/confined blast loading using C-4 charges. Mendeley Data **V1** (2023). https://doi.org/10.17632/zv7y78twd9.1https://data.mendeley.com/datasets/zv7y78twd9/1

26. EUROPLEXUS User's Manual, on-line version. http://europlexus.jrc.ec.europa.eu

27. Cast3m Software. http://www-cast3m.cea.fr/

28. Jones, H., Miller, A.: The detonation of solid explosives: the equilibrium conditions in the detonation wave-front and the adiabatic expansion of the products of detonation. Proc. R. Soc. Lond. Ser. A Math. Phys. Sci. **194**(1039), 480–507 (1948). https://doi.org/10.1098/rspa.1948.0093

29. Wilkins, M., Squier, B., Halperin, B.: The equation of state of PBX 9404 and LX 04-01. Technical Report no. UCRL-7797, Lawrence Radiation Laboratory, USA (1964)

30. Lee, E., Hornig, H., Kury, J.: Adiabatic expansion of high explosive detonation products. Technical report, Univ. of California Radiation Lab. at Livermore, Livermore, CA, USA (1968)

31. Rigby, S.E., Fuller, B., Tyas, A.: Validation of near-field blast loading in LS-DYNA. Proc. ICPS5 2018, 5th International Conference on Protective Structures, Poznan, Poland, August 20-24 (2018)

32. Alia, A., Souli, M.: High explosive simulation using multi-material formulations. Appl. Therm. Eng. **26**, 1032–1042 (2006). https://doi.org/10.1016/j.applthermaleng.2005.10.018

33. Young, D.L.: Time-dependent multi-material flow with large fluid distortion. In: Morton, K.W., Baines, M.J. (eds.) Numerical Methods for Fluid Dynamics. Academic Press, New York (1982)

34. Dobratz, B.M., Crawford, P.C.: LLNL explosives handbook—properties of chemical explosives and explosive simulants. Technical Report UCRL 52997, Lawrence Livermore National Laboratory, University of California, CA, USA (1985). https://doi.org/10.2172/6530310

35. Hallquist, J.O.: LS-DYNA Theory Manual. Livermore Software Technology Corporation, (2006). Livermore Software Technology Corporation. https://www.dynasupport.com/manuals/additional/ls-dyna-theory-manual-2005-beta

36. Harten, A., Lax, P.D., Leer, B.: On upstream differencing and Godunov-type schemes for hyperbolic conservation laws. SIAM Rev. **25**(1), 35–61 (1983). https://doi.org/10.1137/1025002

37. Toro, E.F., Spruce, M., Speares, W.: Restoration of the contact surface in the HLL-Riemann solver. Shock Waves **4**, 25–34 (1994). https://doi.org/10.1007/BF01414629

38. Kristoffersen, M., Minoretti, A., Børvik, T.: On the internal blast loading of submerged floating tunnels in concrete with circular and rectangular cross-sections. Eng. Fail. Anal. **103**, 462–480 (2019). https://doi.org/10.1016/j.engfailanal.2019.04.074

39. Kristoffersen, M., Hauge, K.O., Valsamos, G., Børvik, T.: Blast loading of concrete pipes using spherical centrically placed C-4 charges. Eur. Phys. J. Web Conf. **183**, 01057 (2018). https://doi.org/10.1051/epjconf/201818301057

40. Giordano, J., Jourdan, G., Burtschell, Y., Medale, M., Zeitoun, D.E., Houas, L.: Shock wave impacts on deforming panel, an application of fluid–structure interaction. Shock Waves **14**, 103–110 (2005). https://doi.org/10.1007/s00193-005-0246-9

41. Antoniou, A., Børvik, T., Kristoffersen, M.: Evaluation of automatic versus material test-based calibrations of concrete models for ballistic impact simulations. Int. J. Protect. Struct. (2023). https://doi.org/10.1177/20414196231164431